

Debris disks with multiple absorption features in metallic lines: circumstellar or interstellar origin?

D. Iglesias,^{1,2,3*} A. Bayo,^{1,3} J. Olofsson,^{1,3} Z. Wahhaj,² C. Eiroa,^{4,5} B. Montesinos,^{6,5} I. Rebollido,^{4,5} J. Smoker,² L. Sbordone,² M. R. Schreiber^{1,3} and Th. Henning⁷

¹*Instituto de Física y Astronomía, Facultad de Ciencias, Universidad de Valparaíso, Av. Gran Bretaña 1111, 5030 Casilla, Valparaíso, Chile*

²*European Southern Observatory, Alonso de Córdova 3107, Vitacura, Santiago, Chile*

³*Núcleo Milenio de Formación Planetaria - NPF, Universidad de Valparaíso, Av. Gran Bretaña 1111, Valparaíso, Chile*

⁴*Dpto. Física Teórica, Universidad Autónoma de Madrid, Spain*

⁵*Unidad Asociada AstroUAM-CSIC*

⁶*CAB (CSIC-INTA), P.O. Box 78, 28691 Villanueva de la Canada, Madrid, Spain*

⁷*Max-Planck-Institut für Astronomie (MPIA), Königstuhl 17, D-69117 Heidelberg, Germany*

Accepted XXX. Received YYY; in original form ZZZ

ABSTRACT

Debris disks are second generation dusty disks thought to be devoid of gas. However, this idea has been challenged in the last years by gas detections in some systems. We compiled a database of 301 debris disks and collected high-resolution optical spectra for $\sim 77\%$ of them. From the analysis of these data we identified a group of 23 debris disks presenting several absorption features superimposed to the photospheric Ca II and Na I doublets. These absorptions could be due to circumstellar material or interstellar clouds. In order to discriminate between the two scenarios, we characterized each feature in terms of its radial velocity, equivalent width and column density. Additionally, we searched in the literature for local clouds in the line of sight of the stars, and looked for the presence of similar absorption features in nearby stars. Our study concludes that while all the objects present interstellar absorptions in their spectra, three objects show features more compatible with circumstellar origin: HD 110058 presents a stable circumstellar absorption, while HR 4796 and c Aql present variable absorption features likely due to exocometary activity. The minute-scale variability we detect towards c Aql is the shortest of this kind detected so far. The detection of circumstellar features in these objects is consistent with their near edge-on inclinations. We also provide evidence challenging previous claims of circumstellar gas detections for HR 6507. Given the properties of the sample, we speculate that transient gaseous events must be a common phenomenon among debris disks.

Key words: planetary systems: formation – circumstellar matter – debris disks – ISM: clouds – objects: HR 4796 – c Aql – HD 110058 – HR 6507

1 INTRODUCTION

Planets are believed to form in protoplanetary disks. The mass of these disks is initially composed of 99% gas and 1% dust (ISM-like ratios, Bohlín et al. 1978; but see, among others, Williams & Best 2014). After a few Myrs (e.g. Hernández et al. 2007 and Fedele et al. 2010) these protoplanetary disks evolve from optically thick gas-rich systems into transition disks, and later, at a stellar age of about 10

Myrs, they are transformed into a collection of rocks, dust, planetesimals (and maybe gaseous giant planets) known as debris disks. At this stage, the disk is supposed to be fully depleted of gas due to gas removal processes such as photoevaporation, accretion and radiation pressure (e.g. Pontoppidan et al. 2014 and Alexander et al. 2006 for reviews on volatiles and photoevaporation in protoplanetary disks, respectively). Therefore, the current paradigm is that the majority of debris disks do not harbour gas and contain very little second generation dust produced by collisions among planetesimals; gas giants would have to form during the earlier gaseous stage of the disk; and rocky planets can form or

* E-mail: daniela.iglesias@postgrado.uv.cl

continue to grow later during the gas-poor phase of the disk (Wyatt 2008).

The idea that debris disks should be gas free has been challenged in the past few years by the discovery of a number of debris disks containing some gas detected either in the far-infrared (FIR), infrared (IR), optical or UV wavelengths. These gaseous debris disks have been found mainly around young A type stars, like the well-studied β Pictoris (Brandeker et al. 2004), 49 Ceti (Roberge et al. 2014), HD 32297 (Redfield 2007), HD 172555 (Riviere-Marichalar et al. 2012), HD 21997 (Moór et al. 2011), a few B type stars like σ Her (Chen & Jura 2003) and 51 Oph (Thi et al. 2013), and very few F type stars, HD 181327 and η Corvi (Marino et al. 2016, Marino et al. 2017). Several tracers have been used to this end, for instance CO, C and O emissions at mm wavelengths (Greaves et al. 2016, Kral et al. 2017b), Ca II and Na I absorptions in the optical (Kiefer et al. 2014a) and different C species (C I, C II) and Fe I absorptions in the far UV, among others (Brandeker et al. 2004, Roberge et al. 2006, Roberge et al. 2014).

The possible origin of the gas detected in debris disks has been widely discussed (Moór et al. 2011, Wyatt et al. 2015, Kóspál & Moór 2016, Kral et al. 2017a). In short, it could be residual gas that remained from the earlier gaseous stage of the disk, which would imply that the efficiency of gas removal processes may be lower than we thought. Or, it could be second generation gas, produced by icy comets that, either orbiting or as they approach the star, begin to “evaporate” (or, more correctly, sublimate) and release small amounts of gas. Gas of secondary origin could also be produced by collisions among volatile-rich dust grains or comet-like bodies (Higuchi et al. 2017 and references therein) or even by photon-stimulated desorption of solids (Matthews et al. 2014). These latter two processes could replenish the disk with a stable gaseous component likely to be located in the outer regions of the disk (Brandeker et al. 2004). On the other hand, the idea of the “falling evaporating bodies” (FEBs) has been gaining more acceptance in the last few years, since FEB-like events have been detected (mostly) around A-type stars with debris disks and some shell stars (e.g., Beust et al. 1998, Kiefer et al. 2014c, Eiroa et al. 2016). These events manifest as stochastic absorption features usually at redshifted velocities with respect to the radial velocity of the star. Variable absorption features have been detected over short time windows of hours or night to night as well as over months or years (Barnes et al. 2000, Thébault & Beust 2001, Welsh & Montgomery 2013). One interesting by-product of studying FEBs is posing the question on the cause of such instabilities in the debris disk. A possible cause for such instabilities could be the presence of a larger body like a planetesimal or a planet interfering with the dust transport and evolution of the disk (Beust et al. 1998).

Independently of its origin, the implications of the presence of gas in debris disks are many (see, for a recent review, Hughes et al. 2018). It can change our understanding of gas removal processes by setting new constraints on their efficiency (Williams & Cieza 2011). Particularly for photoevaporation, thought to be the main cause of gas removal in protoplanetary disks (Alexander et al. 2006, Canovas et al.

2017). In addition, gas can influence the morphology of the dust in the disk providing us with a possible answer to the formation of the observed gaps in some debris disks (Lyra & Kuchner 2013). Gas can also imprint changes in the dynamics of the system since even small amounts of gas can drag dust and pebbles (Wyatt 2008); and dust grains can couple to the gas component which acts as a fluid affecting rocky planet formation processes (Fernández et al. 2006, Cleeves et al. 2016, Kenyon et al. 2016). Since the presence of gas can have a strong impact on the formation and evolution of planetary systems it is essential to understand its frequency and how gas detections relate to properties of debris disk systems, such as age, multiplicity, stellar type, metallicity, dust content and disk-planet interaction.

We are currently analysing a robust sample of 301 debris disk (Olofsson et al. in prep.) to learn what percentage of debris disks contain gas, how the gas is physically related to the dust and what properties characterize the stars that possess circumstellar gas in their surrounding debris disks. Instruments such as ALMA and APEX can provide us with a plethora of information about disks besides being able to detect gas emission. However, observing such a large sample with either facility would be extremely expensive in terms of telescope time. In comparison, the analysis of UV-optical ground-based spectra provides a very efficient way to find debris disks with gas to be followed-up with other instruments (Montgomery & Welsh 2012, Welsh & Montgomery 2013, Kiefer et al. 2014a). Just as a simple illustration, integration times of CO surveys with ALMA or APEX are ~ 1 hour per target (Kóspál et al. 2013, Hales et al. 2014), while optical high-resolution high-signal-to-noise-ratio spectroscopic observations of similar targets conforming our sample take only a few minutes or even seconds (in class 2 to 8 meter telescopes). Thus the number of spectra taken during one night ranges from ~ 50 to ~ 100 , depending on the telescope/instrument and the targets.

In order to optimize the search for circumstellar gas in our sample, we have used the method described in Kiefer et al. (2014c), where the presence of gas in the line of sight of debris disks with near edge-on inclinations, is inferred by the identification of (narrow) extra absorption(s) in metallic lines in the UV/optical regime (Ca II H & K and Na I D1 and D2 being particularly good tracers). So far we have been able to collect data for about 77% of our sample and analysing those data, we have found a few particularly interesting objects with multiple gas features which are presented in this paper.

2 DEBRIS DISK SAMPLE

In this paper, we present a sub-sample of 23 gas-rich debris disk candidates characterized by showing gas detections at different radial velocities within our database of observations prior to December 2016. The full sample of debris disks we are observing consists of 301 systems selected from an original list compiled by Olofsson et al. (in prep). The original list, was assembled via a thorough literature search for debris disks that had been observed with the IRS instrument

(Houck et al. 2004) on board of the Spitzer space telescope (Werner et al. 2004). This search resulted in ~ 500 objects that were then filtered down to 301 imposing different criteria on the significance of the excess in the mid-infrared and excluding debris disks that display strong emission features in their IRS spectra (e.g., Olofsson et al. 2012), as these objects are not really representative of “classical” debris disks. It follows then that the selection criteria applied to achieve our database of 301 debris disks are unbiased with respect to disk inclinations as the disks are optically thin and, since most inclinations are unknown, they can be assumed to be following a uniform distribution.

The ages of the systems in the full sample are mostly within the range 10–100 Myrs and most of them are located within distances of less than 200 pc. We are in the process of collecting high-resolution, high-signal-to-noise spectroscopic archival data and obtaining new observations of these objects to analyse the sample in the wavelength ranges covering the Ca II H and K lines at 3968.5 and 3933.7Å, and the Na I D1 and D2 lines at 5895.9 and 5889.9Å. We have been able to collect adequate data for 234 objects in our sample, with $\sim 55\%$ of the selected objects coming from our own observations and the rest from the ESO archive. As mentioned before, the sub-sample presented here was extracted from our database of observations updated up to December 2016.

The main properties of the sub-sample are detailed in Tables 1 and 2. Unless otherwise indicated, most of the stellar parameters reported in Table 2 were retrieved from the Simbad database (Wenger et al. 2000). In particular, distances came from the Tycho-Gaia Astrometric Solution (TGAS) from the Gaia data-release 1 (Gaia Collaboration et al. 2016) or from the Hipparcos new reduction of van Leeuwen (2007) when the former were not available. Luminosities are estimated via SED fitting (assuming the previously mentioned distances) with Kurucz models (Castelli et al. 1997) using VOSA (Bayo et al. 2008). Isochronal ages are estimated with VOSA based on the SED fitted parameters and different sets of isochrones (Siess et al. 2000, Baraffe et al. 1998). The multiplicity column highlights objects reported in the literature to be multiple systems. Note that the large uncertainties in isochronal ages are attributable to uncertainties in the distance to the objects and/or the set of isochrones assumed for the estimates (further discussion on the ages of the sample will be given in Olofsson et al. in prep.). For those objects confirmed to belong to young moving groups (i.e. β 03 Tuc, 66 Psc, ν Hor, HD 24966, HD 54341, η Cha, HD 110058 and HR 6507), we have adopted the literature age commonly assigned to those moving groups (in principle more precise than isochronal dating).

As mentioned before, the 23 candidates presented in this paper have been chosen because they display particularly interesting gas absorption features: they all have not only one, but multiple absorptions at different radial velocities with respect to the star within the 12 years of baseline considered for this paper. Merely by statistical arguments, this multiplicity increases the chances of a circumstellar gas detection, and for the cases that a circumstellar origin for several simultaneous features could be confirmed, it would imply a very interesting disk configuration and/or geome-

Table 1. Sub-sample of gas-rich debris disk candidates with multiple absorption features and their respective coordinates.

Name	HD Id	R.A. [J2000]	Dec. [J2000]
β 03 Tuc	HD 3003	00:32:43.9	-63:01:53.4
66 Psc	HD 5267	00:54:35.2	+19:11:18.3
ν Hor	HD 17848	02:49:01.5	-62:48:23.5
HD 24966	HD 24966	03:56:29.4	-38:57:43.8
HD 290540	HD 290540	05:31:31.4	-01:49:33.3
HD 36444	HD 36444	05:31:40.5	-01:07:33.3
HD 290609	HD 290609	05:33:05.6	-01:43:15.5
HR 1919	HD 37306	05:37:08.8	-11:46:31.9
HD 54341	HD 54341	07:06:20.9	-43:36:38.7
HD 60856	HD 60856	07:35:56.9	-14:42:39.0
HR 3300	HD 71043	08:22:55.2	-52:07:25.4
η Cha	HD 75416	08:41:19.5	-78:57:48.1
HD 92536	HD 92536	10:39:22.8	-64:06:42.4
3 Crv	HD 105850	12:11:03.8	-23:36:08.7
HD 106036	HD 106036	12:12:10.3	-63:27:14.8
HR 4796	HD 109573	12:36:01.0	-39:52:10.2
HD 110058	HD 110058	12:39:46.2	-49:11:55.5
HD 112810	HD 112810	12:59:59.9	-50:23:22.5
HD 126135	HD 126135	14:24:43.9	-40:45:18.6
HD 141378	HD 141378	15:48:56.8	-03:49:06.6
HD 141327	HD 141327	15:49:43.1	-32:48:29.8
HR 6507	HD 158352	17:28:49.7	+00:19:50.3
cAql	HD 183324	19:29:00.9	+01:57:01.6

try. For instance, a disk containing several gas rings at different distances from the star or different populations of exocomets, which would require further study and possible follow-up with high angular resolution instruments like ALMA.

3 SPECTROSCOPIC DATA

We performed observations with FEROS (Kaufer et al. 1999) on the MPG/ESO 2.2m telescope at the La Silla Observatory in Chile and UVES (Dekker et al. 2000) on the VLT UT2 telescope at Paranal Observatory, Chile. We also queried the ESO archive searching for all relevant high-resolution spectra covering the blue-optical wavelength ranges. In particular data from HARPS (Mayor et al. 2003), UVES and FEROS instruments were searched for¹.

3.1 New data

3.1.1 FEROS observations

We performed observations with the FEROS Échelle spectrograph for the objects listed in Table 3². The instrument choice is motivated by its characteristics: large wavelength range (the complete optical spectral region from $\sim 3500\text{\AA}$ to

¹ The list of programme IDs can be found in the Acknowledgements.

² Programme IDs: 094.A-9012(A), 096.A-9018(A) and 099.A-9004(A)

Table 2. Stellar parameters for the sample.

Name	$v_{\text{sin}i}$ [km.s ⁻¹]	Spectral Type	radV [km.s ⁻¹]	distance [pc]	Isochronal Age [Myr]	Literature Age [Myr]	$\log(L_{\text{bol}}(L_{\odot}))$ [dex]	Multi- plicity
β 03 Tuc	93	A0V	7.70±0.80	45.56±0.39 ^{4b}	115.48± ^{137.30} _{115.48}	30.0 ^d ± ^{0.0} _{20.0}	1.19± ^{0.01} _{0.01}	✓ ^j
66 Psc	144	A1Vn	8.50±2.80	108.11±7.48 ^b	5.00± ^{0.98} _{0.31}	200 ^e	1.46± ^{0.06} _{0.07}	✓ ^k
ν Hor	143.7	A2V	30.90±2.00	52.13±1.76 ^c	529.02± ^{103.10} _{129.08}	100 ^e	1.23± ^{0.04} _{0.05}	–
HD 24966	–	A0V	–	105.82±4.03 ^b	195.41± ^{102.01} _{195.41}	10 ^e	1.13± ^{0.04} _{0.04}	–
HD 290540	–	A2	–	357.32±54.90 ^c	11.57± ^{338.74} _{11.57}	112 ^f	1.23± ^{0.12} _{0.17}	–
HD 36444	–	B9V	–	458.20±98.20 ^c	4.33± ^{603.23} _{1.33}	101 ^f	1.57± ^{0.16} _{0.26}	–
HD 290609 ¹	–	A0	–	23.86±11.43 ^b	–	5 ^g	2.41± ^{0.00} _{0.00}	–
HR 1919	148.1	A1V	23.00±0.70	70.76±4.15 ^c	28.52± ^{307.72} _{28.52}	453 ^f	1.10± ^{0.06} _{0.07}	–
HD 54341	–	A0V	–	102.35±3.77 ^b	7.94± ^{391.30} _{0.97}	10 ^e	1.34± ^{0.05} _{0.05}	–
HD 60856	44	B5V	31.20±1.90	363.83±88.54 ^c	2.19± ^{93.55} _{0.20}	196 ^f	1.84± ^{0.05} _{0.29}	–
HR 3300	224	A0V	22.50±1.10	70.03±1.13 ^b	710.26± ^{111.03} _{701.81}	404 ^f	1.11± ^{0.02} _{0.02}	–
η Cha	296 ^a	B8V	14.00±7.40	94.97±1.44 ^b	3.09± ^{297.86} _{0.09}	6.0 ^d ± ^{1.0} _{0.0}	1.80± ^{0.03} _{0.03}	–
HD 92536	–	B8V	10.00±1.00	145.13±8.75 ^c	4.04± ^{0.49} _{0.90}	231 ^f	1.66± ^{0.07} _{0.08}	–
3 Crv	126.8	A1V	11.00±4.20	58.82±1.94 ^b	907.37± ^{92.96} _{899.21}	465 ^f	1.14± ^{0.04} _{0.05}	–
HD 106036	–	A2V	7.70±1.30	99.00±3.87 ^c	463.25± ^{238.95} _{463.25}	17 ^h	0.98± ^{0.05} _{0.05}	–
HR 4796	152.0	A0V	7.10±1.10	72.78±1.75 ^b	69.59± ^{30.85} _{69.59}	378 ^f	1.56± ^{0.05} _{0.05}	✓ ^l
HD 110058	–	A0V	5.00±1.20	188.76±34.11 ^c	560.29± ^{48.08} _{560.29}	10 ^e	1.24± ^{0.19} _{0.34}	–
HD 112810	82	F3/5IV/V	4.20±1.20	134.60±7.22 ^c	1997.73± ^{1012.17} _{1997.73}	10 ⁱ	0.46± ^{0.05} _{0.05}	–
HD 126135	–	B8V	12.00±6.00	165.02±16.34 ^b	5.00± ^{692.27} _{0.80}	103 ^f	1.44± ^{0.10} _{0.08}	–
HD 141378	107	A5IV-V	-16.40±2.00	55.54±2.32 ^c	10.05± ^{0.65} _{0.15}	587 ^f	0.99± ^{0.04} _{0.04}	–
HD 141327	–	B9V	-5.10±2.40	213.29±22.48 ^c	4.88± ^{794.54} _{0.88}	196 ^f	1.46± ^{0.09} _{0.12}	–
HR 6507	180	A8Vp	-36.10±2.00	59.63±0.93 ^b	7.83± ^{0.22} _{0.72}	600 ^e	1.17± ^{0.01} _{0.01}	–
cAql	110	A0IVp	12.00±4.30	61.20±1.35 ^b	60.55± ^{0.00} _{60.55}	506 ^f	1.29± ^{0.05} _{0.06}	–

^aZorec & Royer (2012), ^bvan Leeuwen (2007), ^cTGAS, ^dTorres et al (in prep.), ^eRhee et al. (2007), ^fGontcharov (2012), ^gHernández et al. (2006), ^hMittal et al. (2015), ⁱBallering et al. (2013), ^jDommanget & Nys (2002), ^kDocobo & Ling (2007), ^lJura et al. (1993).

¹Distances reported for this object range from ~ 24 pc (van Leeuwen 2007) to ~ 775 pc (Kharchenko 2001); both of those estimates report huge uncertainties (above 50%), and propagate to unrealistic luminosities and thus isochronal ages. For this reason we do not include this object in any comparative analysis that involves age, luminosity and/or distance.

$\sim 9200\text{\AA}$ in only one exposure), high resolution ($R = 48,000$) and high spectral stability, which makes it suitable for detecting narrow absorption features in a wide variety of spectral lines. Spectra of these objects were taken on the nights listed in Table 3 with exposure times computed with the online FEROS Exposure Time Calculator³ to obtain a signal-to-noise ratio (S/N hereafter) of about ~ 150 around the blue wavelength range. Standard calibrations were taken and the ESO pipeline with the default parameters was used to reduce the data. The reduced spectra were corrected for heliocentric velocity shifts and telluric contamination (see Sec. 3.3).

3.1.2 UVES observations

We obtained UVES spectra in service mode during periods P96⁴ and P97⁵ for the objects listed in Table 3. Data from P96 were observed with the blue arm centred at 4370 \AA and with a spectral coverage of 3731–4999 \AA and data from P97 were observed in dichroic mode with the blue arm centred at 3900 \AA and the red arm centred at 5800 \AA , covering the spectral ranges 3282–4562 \AA and 4726–6835 \AA , respectively. The narrowest slits were used in order to achieve the maximum resolution possible; the 0.4'' slit in the blue arm and

the 0.3'' slit in the red arm, yielding resolutions of 80,000 and 110,000, respectively. Exposure times were computed with the online UVES Exposure Time Calculator⁶ aiming to obtain a S/N ~ 150 (achieved for most of the spectra) around the blue wavelength range under thick (very low transparency) sky conditions. Standard calibrations were also taken and the ESO pipeline with the default parameters was used to reduce the data. The spectra were a posteriori corrected for telluric contamination (see Sec. 3.3).

3.2 Archival data

We queried the ESO archive looking for optical spectra with resolution high enough to detect narrow absorption features with widths of $\sim 0.1\text{\AA}$. This restricted the instruments to HARPS, UVES and FEROS. Our targets have been observed multiple times (e.g., searching for planets via radial velocity variations), hence we found a large number of spectra (from one spectrum up to 3000 spectra). Consequently, a considerable fraction of our dataset ($\sim 35\%$ of the full sample) comes from different archives. In fact, 16 of our debris disks with multiple features were identified with these observations.

³ <https://www.eso.org/observing/etc/bin/gen/form?INS.NAME=FEROS+INS.MODE=spectro>

⁴ Programme ID: 096.C-0238(A)

⁵ Programme IDs: 097.C-0409(A) and 097.C-0409(B)

⁶ <https://www.eso.org/observing/etc/bin/gen/form?INS.NAME=UVES+INS.MODE=spectro>

Table 3. Number of spectra for each star per date, instrument, ESO observing period and dates of observations. Observations from our programmes are flagged with a *.

Name	Number of Spectra	Instrument	Period	Observation dates
β 03 Tuc	6, 4, 2, 2, 2	HARPS	P73, P75, P77, P77, P77	2004-09-30, 2005-08-19, 2006-05-[20, 25, 26]
	2, 2, 2, 2, 2, 2	HARPS	P84, P84, P84, P84, P84, P84	2009-11-[12, 13, 14, 15], 2009-12-[05, 08]
	2, 2, 2, 2	HARPS	P85, P86, P86, P87	2010-07-07, 2011-01-[06, 07], 2011-07-23
66 Psc	1, 1	FEROS	P96, P96	2015-10-[23, 24]*
	1, 2	UVES	P96, P97	2015-11-14*, 2016-07-23*
ν Hor	6, 2, 2	HARPS	P75, P75, P77	2005-08-19, 2005-09-09, 2006-09-11
	2, 2, 2, 6, 2	HARPS	P80, P80, P80, P94, P94	2007-12-[05, 06, 10], 2015-01-[18, 20]
HD 24966	1	FEROS	P96	2016-01-04*
	2, 2, 2	UVES	P97, P97, P97	2016-07-23*, 2016-08-[21, 29]*
HD 290540	1, 1	FEROS	P96, P96	2016-01-[03, 04]*
HD 36444	1	FEROS	P96	2016-01-04*
HD 290609	1	FEROS	P96	2016-01-04*
HR 1919	4, 2, 2, 2, 2, 2	HARPS	P76, P76, P76, P76, P76, P76	2006-02-[08, 09, 10, 11, 13], 2006-03-12
	2, 2, 2, 2	HARPS	P78, P80, P80, P80	2006-11-18, 2007-12-[05, 06, 10]
	2, 1, 1	FEROS	P96, P96, P96	2015-10-23*, 2016-03-[28, 29]*
HD 54341	3, 1	HARPS	P94, P94	2015-01-[19, 20]
HD 60856	1	FEROS	P96	2016-01-04*
HR 3300	6, 2, 2	HARPS	P94, P4, 94	2015-01-[18, 20, 21]
	1, 2, 3, 3	FEROS	P82, P82, P82, P88	2008-11-[18, 21, 22], 2011-12-07
	1, 1	FEROS	P96, P96	2015-10-23*, 2016-03-26*
η Cha	2, 3	UVES	P66, P66	2001-02-[16, 18]
	3, 6, 2	HARPS	P60, P94, P94	2005-02-12, 2015-01-[19, 20]
	2, 2, 5	FEROS	P60, P60, P60	2006-10-24, 2006-12-08, 2007-01-01
	4, 4, 4	FEROS	P60, P60, P60	2007-2-[16, 23, 24]
	1, 1, 1	FEROS	P84, P84, P84	2009-11-30, 2009-12-[05, 07]
	1, 1, 1, 1, 1, 1	FEROS	P84, P84, P84, P84, P85, P85	2010-01-[27, 28, 29, 30], 2010-06-[01, 14]
HD 92536	3, 3, 2, 1	HARPS	P94, P94, P94, P94	2015-01-[18, 19, 20, 21]
3 Crv	6, 2, 2, 2, 2	HARPS	P77, P77, P77, P80, P84	2006-05-[20, 21, 25], 2007-12-10, 2009-12-05
	4, 2, 6, 2	HARPS	P85, P85, P86, P86	2010-07-[08, 09], 2011-01-[04, 07]
	2, 2, 2, 2	HARPS	P86, P86, P86, P87	2011-02-[4, 5, 6], 2011-07-21
	1, 1	FEROS	P96, P96	2016-03-[26, 29]*
HD 106036	2	UVES	P96	2016-02-21*
HR 4796	74, 152, 76, 76, 92, 16	UVES	P68, P79, P79, P79, P79, P79	2002-01-19, 2007-05-[07, 08, 13, 14, 15]
	2, 3, 2, 3	HARPS	P80, P94, P94, P94	2007-12-06, 2015-01-[19, 20, 21]
	1, 1, 2, 1, 1	FEROS	P79, P79, P79, P79, P79	2007-03-09, 2007-05-[01, 04, 12, 27]
	2, 3, 4, 3	FEROS	P96, P96, P96, P96	2016-03-[26, 27, 28, 29]*
HD 110058	2, 1	FEROS	P84, P87	2010-01-31, 2011-04-16
	6, 2, 2, 2	HARPS	P94, P94, P94, P94	2015-01-[18, 19, 20, 21]
HD 112810	2	UVES	P96	2016-03-23*
HD 126135	1, 1, 2	HARPS	P94, P94, P94	2015-01-[18, 20, 21]
HD 141378	1	FEROS	P92	2014-02-18
HD 141327	1, 1, 2	FEROS	P79, P81, P82	2007-04-02, 2008-04-01, 2009-02-06
HR 6507	4, 2, 2, 2	HARPS	P75, P77, P77, P77	2005-08-20, 2006-05-[20, 25], 2006-09-12
	2, 5, 2, 2	HARPS	P80, P80, P84, P84	2008-03-[17, 21], 2010-07-[08, 09]
	6	UVES	P83	2009-04-16
c Aql	10, 38	UVES	P79, P87	2007-06-30, 2011-05-27
	1, 1, 1	FEROS	P83, P83, P83	2009-06-[02, 03], 2009-08-24
	1, 1, 1	FEROS	P85, P85, P85	2010-07-22, 2010-08-[23, 31]

3.2.1 HARPS data

HARPS is an echelle spectrograph fed by a pair of fibres, one of them collects the star light, while the second is used to either record simultaneously a Th-Ar reference spectrum or the background sky. HARPS spectra covers the wavelength range 3780–6910Å, has a spectral resolution of 120,000 and has been optimised for mechanical stability, which makes it ideal for our study. We retrieved several epochs of HARPS data for the debris disks listed in Table 3. All these observations were already reduced with the ESO pipelines and corrected for heliocentric radial velocity shifts, and we then corrected for telluric contamination (see Sec. 3.3).

3.2.2 UVES data

Additional to the HARPS data, we found a considerable number of UVES observations for our sample (see Table 3). UVES is a two-arm cross-dispersed echelle spectrograph, its blue arm covers the wavelength range 3000–5000Å and the red arm covers 4200–11000Å. Overall, the spectral coverage depends on the instrumental set-up used for the observations since UVES allows the use of dichroic beam splitters, but in general we have spectra covering the ranges 3043–3916Å, 3236–4563Å, 3731–4999Å, 4549–6686Å, 4726–6835Å and 6650–10426Å. These UVES data had already been reduced with dedicated ESO pipelines but additional corrections of

heliocentric radial velocity shifts and telluric contamination were necessary.

3.2.3 FEROS data

We also retrieved FEROS archival data for some of our targets (Table 3). Similarly to the HARPS data, the FEROS observations were reduced with the available instrument pipelines and corrected for heliocentric radial velocity shifts. Posterior corrections for telluric contamination were performed.

3.3 Telluric lines correction

The red domain of the spectra contains many telluric absorption features mostly due to water vapour, O_2 and O_3 . Since one of our main tracers is the sodium doublet at 5895.9 and 5889.9Å, it is imperative to perform a correct subtraction of telluric contamination. To this end, we used *Molecfit*⁷ (Smette et al. 2015, Kausch et al. 2015), a tool developed to correct observations for telluric absorption which can be used for any kind of spectra without the need to observe a standard star. We used the wavelength range 5902.5–5927.0Å to fit the continuum but excluded gas absorption features to ensure that they do not affect our best-fitting result. We applied these corrections to every epoch for all the objects except for HD 106036 and HD 112810 which spectra did not cover the red wavelength range. We successfully removed telluric absorptions and reduced them to the noise level (i.e. they were reduced by about 99%). An example of the telluric correction is shown in Figure 1.

4 METHODS AND RESULTS

We analysed the calcium H & K lines at 3968.47 and 3933.66Å and the sodium D1 & D2 lines at 5895.92 and 5889.95Å, respectively. The aim is to detect narrow absorption lines superimposed on the photospheric line. These “extra” absorption lines indicate the presence of gas in the line of sight of the star. To determine the nature of the gas we followed different approaches, that we detail in the following sub-sections.

The first step in our analysis is to measure the radial velocity of the stars. Afterwards, we determined the photospheric contribution for each line either by performing spectral synthesis or by finding a “spectral twin”. Then, we identified additional (stable or transient) components by removing the photospheric contribution before characterizing their properties.

Additionally, we also searched for signatures of Diffuse Interstellar Bands (DIBs), compared the radial velocity of

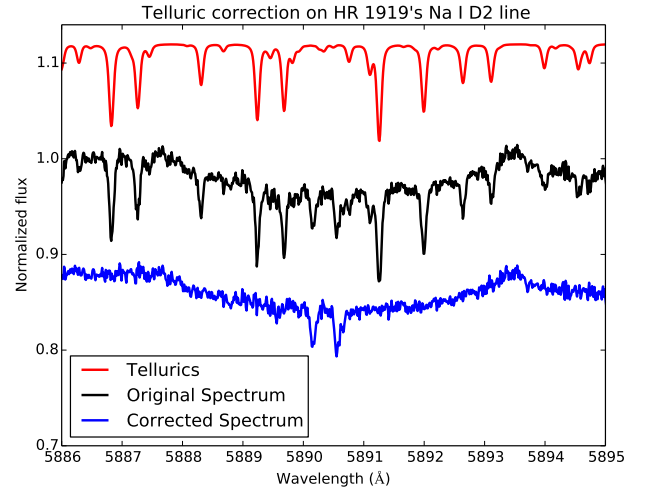


Figure 1. Example of telluric correction in HR 1919’s Na I D2 line. Telluric lines modeled by molecfi in red, original spectrum in black, and corrected spectrum in blue. The different spectra are shifted with respect to each other for clarity.

the absorption features to the radial velocities of known local clouds and searched for similar extra absorption lines in nearby stars to better assess their nature.

4.1 Radial velocities

Since five of our objects did not have any reported radial velocity measurements in the literature, we performed our own estimates for all objects aiming at a homogeneously determined set of values and to assess the accuracy of our results.

In a first attempt to obtain the radial velocities, we computed the cross correlation function for every epoch of each object using a synthetic model as a template. Unfortunately, since most of our objects are fast rotators, their absorption lines have very wide profiles, and we did not obtain consistent results between all the epochs, with dispersions up to 30 km.s^{-1} . Therefore, we decided to take a different approach and use a simpler but, in this case, more suitable technique. For every epoch of each object we fit Lorentzian profiles to the most prominent absorption lines in our spectra: $H\alpha$, $H\beta$, $H\gamma$ and $H\delta$. We excluded $H\epsilon$ because it is blended with the Ca II H line. We used a range of 1000 km.s^{-1} for the profile fitting of each (previously normalized) line in velocity space and obtained the radial velocity of the line from the position of the profile with respect to the rest frame.

In order to address possible changes in the estimates of radial velocities due to activity, we checked all our objects for emission features in the Balmer lines (not only for emission dominated lines, but also for shallow core emissions). Only one object, namely HD 60856, presents emission features in these lines. This emission is dominating the full line in the

⁷ <http://www.eso.org/sci/software/pipelines/skytools/molecfi>

Table 4. Stellar parameters determined from the synthetic model fitting and radial velocity estimates computed as described in Section 4.1. Radial velocity of stars in multiple or binary systems are flagged with *. The typical uncertainties for the estimates of $v\sin i$ and $T_{\text{eff}}(\text{Ca II K})$, are of $\sim 5 \text{ km.s}^{-1}$ and 5-10%, respectively. Dispersion values come from the measurements in the four different lines or from the grid step size (entries marked with ^g) when the four lines yielded the same values.

Name	$v\sin i$ [km.s^{-1}]	radV [km.s^{-1}]	$T_{\text{eff}}(\text{Ca II K})$ [K]	$\log g$ [dex]	[Fe/H]
β 03 Tuc	100	$6.05 \pm 1.60^*$	9550	4.00 ± 0.50	$+0.17 \pm 0.20$
66 Psc	150	$4.32 \pm 2.66^*$	10750	3.90 ± 0.23	-0.38 ± 0.54
ν Hor	140	13.58 ± 1.67	8300	4.25 ± 0.25	-0.20 ± 0.31
HD 24966	210	15.70 ± 3.15	9250	4.38 ± 0.22	-0.03 ± 0.58
HD 290540	200	27.26 ± 3.12	10500	4.25 ± 0.25	-0.88 ± 0.22
HD 36444	360	26.72 ± 4.50	10250	4.00 ± 0.35	-0.62 ± 0.65
HD 290609	100	25.87 ± 1.65	10500	3.88 ± 0.41	-0.07 ± 0.26
HR 1919	140	23.49 ± 1.28	8800	4.15 ± 0.38	-0.12 ± 0.22
HD 54341	140	41.03 ± 0.95	10500	4.50 ± 0.25^g	-0.12 ± 0.22
HD 60856	40	34.78 ± 3.58	14000	4.12 ± 0.22	-0.38 ± 0.41
HR 3300	210	22.35 ± 0.72	9550	4.25 ± 0.25	$+0.10 \pm 0.37$
η Cha	280	15.21 ± 1.41	11750	3.75 ± 0.25	-0.88 ± 0.22
HD 92536	180	15.45 ± 0.44	11150	3.88 ± 0.41	-0.45 ± 0.55
3 Crv	130	14.41 ± 1.09	8500	4.12 ± 0.22	$+0.17 \pm 0.41$
HD 106036	160	9.37 ± 2.34	9000	4.50 ± 0.25^g	$+0.00 \pm 0.25^g$
HR 4796	150	$5.35 \pm 2.94^*$	9800	4.25 ± 0.25	-0.07 ± 0.26
HD 110058	150	11.20 ± 0.81	9000	4.03 ± 0.36	-0.33 ± 0.47
HD 112810	–	5.25 ± 2.24	–	–	–
HD 126135	310	11.73 ± 0.67	11250	3.88 ± 0.41	-0.62 ± 0.65
HD 141378	80	-14.68 ± 2.62	8750	4.50 ± 0.25^g	$+0.42 \pm 0.13$
HD 141327	250	-4.65 ± 2.40	10550	4.00 ± 0.35	-0.50 ± 0.50
HR 6507	140	-36.13 ± 2.49	7750	4.25 ± 0.25	$+0.28 \pm 0.13$
c Aql	90	17.29 ± 2.61	9700	4.35 ± 0.26	-0.57 ± 0.49

case of H α and thus it was not possible to model the photospheric profile. Therefore, only for this object, we decided to exclude H α from the radial velocity measurements. In addition, we bootstrapped each of the remaining Balmer lines to estimate the impact of a core emission in our fitting procedure. The standard deviation for the radial velocity from this procedure with 1000 realizations was $\sim 1.6 \text{ km.s}^{-1}$. This object has only one epoch of observations, therefore our estimated uncertainty for the radial velocity takes into account the individual line fitting uncertainties and the dispersion found among the different lines.

For all the other objects, since the cores of the lines appeared purely photospheric, we averaged over all the epochs and lines, and the uncertainties were derived propagating the estimated errors.

In most cases, our radial velocity measurements are in good agreement with the ones found in the literature (see Table 2), having average differences of $\sim 3 \text{ km.s}^{-1}$. However, the radial velocity value we determined for ν Hor differed by $\sim 17 \text{ km.s}^{-1}$ with respect to the literature. We compared both radial velocity values when fitting Kurucz (Castelli et al. 1997) models and concluded that our estimate provides a better match to our data. In general, although differences with the literature were relatively small, in the model fitting process we always obtained a better fit when shifting the model to our own estimates of radial velocity. In any case, the large difference found for ν Hor is not that surprising given the high dispersion in the measurements provided from different datasets in Wilson (1953), the reference adopted in Simbad. Finally, we must also note that, for the whole sample, no significant shifts were found between

epochs, obtaining velocity dispersions per object of the order of $\sim 2 \text{ km.s}^{-1}$. Our resulting radial velocity estimates are shown in Table 4.

4.2 Spectral synthesis

For most objects (except HD 112810, see Sec. 4.3), we used Kurucz models (Castelli et al. 1997) to fit and normalize the photospheric absorption, thus isolating the additional absorption lines. The models were computed using the spectral synthesis codes SYNTHÉ and ATLAS 9 (Sbordone et al. 2004).

For each line we computed the normalized median spectrum from all the epochs, to use it as a robust reference for the fitting process. Since the radial velocity dispersion along all the epochs is small, the median can be used as a good reference. For each of the median spectrum, the uncertainties are derived using the standard deviation of all epochs if there are more than 2 epochs. For objects with only one or two epochs, the pipelines do not always provide uncertainties. Therefore, for each wavelength point, we estimate the standard deviation in a moving box with a width of 33 wavelength points. Then, we computed a grid of models with different stellar parameters for the wavelength ranges containing the Ca II and Na I doublets. The free parameters that can be investigated in the modelling process are: the effective temperature T_{eff} , the surface gravity $\log g$, the metallicity [Fe/H], turbulent velocity, additional turbulence, opacity threshold for the lines, and projected rotational velocity $v\sin i$. We adopted standard values for the turbulent velocity, additional turbulence and opacity threshold; and explored

Table 5. Adopted and explored values for the parameters of the Kurucz models.

Parameter	Values
Turbulent Velocity	2.0 km.s ⁻¹
Additional Turbulence	0.0 km.s ⁻¹
Opacity Threshold	0.001
T _{eff}	6000–13000 K, with Δ=250 K
log <i>g</i>	[3.5, 4.0, 4.5]
[Fe/H]	[-1.0, -0.5, 0.0, +0.2, +0.5]
<i>v</i> sin <i>i</i>	20–400 km.s ⁻¹ , with Δ=10 km.s ⁻¹

the remaining parameters: T_{eff}, log *g*, [Fe/H] and *v*sin*i*. Table 5 summarizes the fixed values and range of parameters that we explored in the fitting process. Those ranges were chosen according to previous estimates available in the literature. Our model fitting procedure consists of a simple two-step χ^2 minimization. The fits were performed for each line independently since, possibly due to non-Local Thermodynamic Equilibrium (non-LTE) effects (Mashonkina et al. 2000, Plez 2013 and Sitnova et al. 2017), it is hardly possible to obtain good matches for all of them simultaneously. The only parameter determined using all the lines at once is *v*sin*i*. The first step consists of estimating approximate values for all the parameters, within a coarse grid of models. The step sizes are reported in Table 5. Afterwards, we used a simplex downhill method with finer interpolations for T_{eff} and log *g*, with steps of 50 K and 0.1 dex, respectively. To avoid local minima, we repeated the simplex downhill algorithm several times, initializing it from different regions of the parameter space that yielded similar (a factor 2 with respect to the minimum) χ^2 values in the coarse grid. The convergence criterion for the downhill algorithm was set to an improvement in the goodness of fit by 10⁻⁴. Given that Ca II K is the most sensitive photospheric temperature tracer among all the lines studied (Gray & Corbally 2009), in Table 4 we report as the best fitting temperature the one obtained for that line. A rather conservative confidence interval is estimated from all the models that returned a relative change in χ^2 smaller than 50% compared to the best fitting model. On the other hand, for log *g* and [Fe/H], we provide an average of the values obtained for the four lines, and the associated uncertainties correspond to their standard deviations.

Once the best fitting model per line is found, it is used to isolate the extra absorption lines from the photospheric profile. The best fits for each objects and lines are displayed in Figures A1 to A4.

We were able to find matching photospheric models for all the objects, and the resulting parameters are consistent with their spectral types from the literature. The only exception is HD 112810, which is an F3/5IV/V spectral type according to the literature and the only F-type star within the sample presented in this paper (we further discuss this object in Section 4.3). Otherwise, for each individual object, the dispersion in T_{eff} for the four different lines is of the order of ~ 300 K, which is expected when accounting for non-LTE effects (Przybilla et al. 2011, Plez 2013 and Sitnova et al. 2017).

4.3 Spectral twins

As an alternative to the synthetic spectrum, we also performed a search for the closest spectral match within all the objects in our sample for which we have spectra (i.e. 234 objects). In particular, we compared the median spectrum (the same as the reference spectrum) of each candidate against the median spectrum of each object in the sample with similar spectral types. We used a range of 11 subtypes (e.g. between A0 and F0 for an A5 candidate) for the spectral twin search.

Similar to the synthetic model fit, we selected the best fitting “template” in terms of minimum χ^2 . The only difference is that in the χ^2 calculation we neglected the wavelength regions containing the 10% most distant data points between the two spectra being compared, in order to avoid a bias induced by the presence of extra features in either spectra.

In the case of HD 112810, since we were not able to find a satisfactory Kurucz model, we used the spectral twin we found for the object as a photospheric model to isolate the absorption feature. As can be seen in Fig. 2, HD 15115 is a good match to the spectrum of HD 112810.

4.4 Identification and characterization of features

We started by normalizing the reference (median) spectrum by the synthetic model (or spectral twin for HD 112810) to isolate the extra absorption features. In some cases when the model is not a perfect match (often the case in the wings of the photospheric lines), the normalized spectrum shows a “wavy” pattern, that makes the characterization of the extra features more challenging. In those cases we performed a polynomial fit to the normalized spectrum to remove this wavy pattern.

Afterwards, we performed Gaussian fitting to each of the extra absorption features in order to derive radial velocities, equivalent widths and apparent column densities. In the case of blended absorption lines, we modelled a combined Gaussian profile with the minimum number of Gaussians that would finely fit the profile. We only considered as “real absorption features” those with significance above 3 σ over the residual spectrum. We considered a feature to be “the same” as that present in another line of the same object when the absolute difference of the radial velocity of both features is $\leq 2\sigma$, where $\sigma = \sqrt{\sigma_1^2 + \sigma_2^2}$, being σ_1 and σ_2 the uncertainty of the radial velocity of each feature.

Radial velocities and equivalent widths were estimated from the best Gaussian(s) fit. In addition, apparent column densities were estimated following Savage & Sembach (1991) and using the oscillator strength values *f* from Morton (1991). We checked our own estimates for three stars against results produced by the Vapid code (Voigt Absorption Profile Interstellar Dabbler Howarth et al. 2002, which can model interstellar absorption lines) and they agreed within the uncertainties. Apparent column density (CaII/NaI) ra-

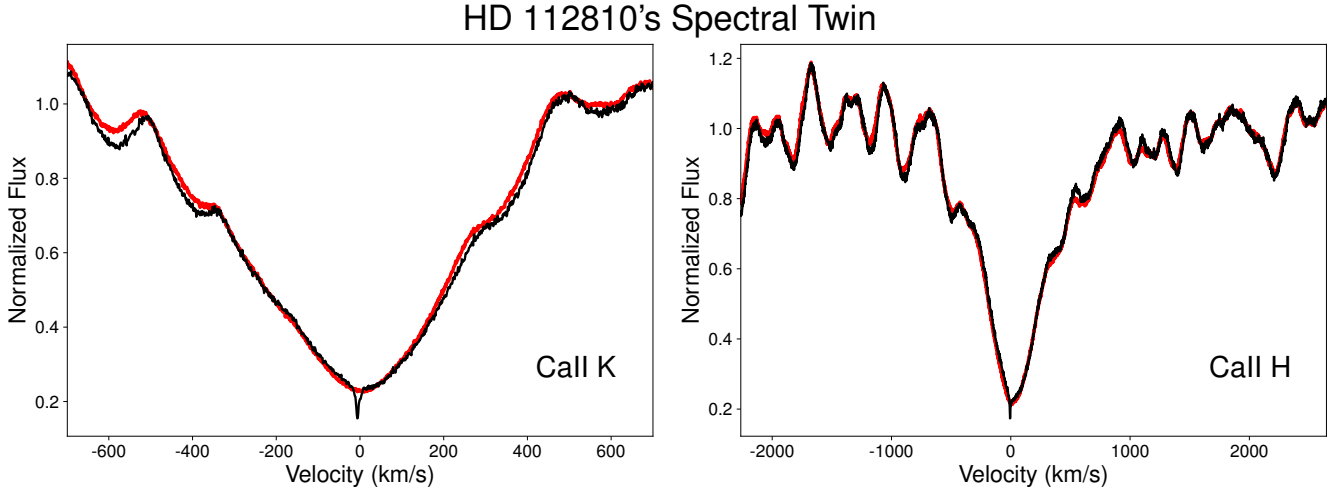


Figure 2. Spectral twin found for HD 112810 (in black): the F4IV type star HD 15115 (in red). The radial velocities of both stars have been shifted to zero for a better comparison. No additional broadening has been added to the spectra of any of the two objects.

tios were also computed as they can help to discriminate the origin of the features.

We noticed that for some of the objects with Na I column densities exceeding 12.0, the column density in Na I D1 is larger by about 0.2 dex than the one for Na I D2. This is likely caused by saturation, i.e. the line with the weaker transition yields a higher column density. Although this problem affects the precision of the measurements in these particular cases, in the end it does not strongly bias the final verdict on the origin of the gas, since we have performed several independent kinds of analysis in order to reach our conclusions.

The parameters for each line and feature are presented in Table 6. The average radial velocity of each feature and their $N(\text{Ca II}/\text{Na I})$ are shown in Table 8. As can be seen in the Tables, the range of properties is very wide, including blue and red-shifted components, weak and intense features, either Ca II or Na I rich. The detailed discussion on the impact of these parameter in determining the origin of the gas responsible for the feature is left to Section 5.

Table 6: Absorption feature parameters. Heliocentric radial velocity, apparent column density and equivalent width of the features present in each line. Uncertainties for the radial velocities are in the order of 2.3 km.s^{-1} for the CaII lines and 1.5 km.s^{-1} for the NaI lines. Apparent column densities and equivalent widths have uncertainties of 3–4% for the CaII lines and 1–2% for the NaI lines.

Name	CaII K			CaII H			NaI D1			NaI D2		
	radV [km.s^{-1}]	$\log_{10} N$ [cm^{-2}]	EW [$\text{m}\text{\AA}$]	radV [km.s^{-1}]	$\log_{10} N$ [cm^{-2}]	EW [$\text{m}\text{\AA}$]	radV [km.s^{-1}]	$\log_{10} N$ [cm^{-2}]	EW [$\text{m}\text{\AA}$]	radV [km.s^{-1}]	$\log_{10} N$ [cm^{-2}]	EW [$\text{m}\text{\AA}$]
β 03 Tuc	-12.23	9.78	0.52	–	–	–	–	–	–	-10.21	9.24	0.34
	-3.52	10.03	0.91	-4.41	10.14	0.60	-3.50	10.50	3.10	-3.51	10.51	6.25
	1.89	10.57	3.19	1.72	10.29	0.84	–	–	–	3.18	9.64	0.85
66 Psc	-5.14	11.10	10.38	-6.01	11.05	4.72	-5.83	11.28	17.49	-5.85	11.27	31.64
	2.58	10.25	1.51	–	–	–	-1.44	10.48	2.93	0.32	10.18	2.93
	10.74	10.56	3.09	–	–	–	12.23	9.71	0.51	–	–	–
ν Hor	5.41	10.55	3.04	4.18	10.35	0.96	3.86	9.52	0.33	2.97	9.78	1.20
	13.03	10.46	2.46	12.35	10.36	1.00	13.02	10.02	1.03	12.57	9.86	1.43
	–	–	–	–	–	–	-8.91	9.67	0.46	-9.27	9.41	0.51
HD 24966	-13.10	10.52	2.79	–	–	–	–	–	–	–	–	–
	17.00	10.89	6.55	15.04	10.71	2.23	15.34	9.90	0.78	15.32	9.87	1.45
	30.21	10.37	1.98	–	–	–	–	–	–	34.08	9.55	0.69
HD 290540	9.51	11.61	32.77	9.27	11.50	13.29	9.09	11.45	26.23	9.26	11.44	49.67
	23.96	12.00	64.17	24.15	12.14	49.91	23.47	12.13	98.75	23.56	11.96	123.98
	33.78	11.13	11.33	37.80	10.67	2.02	35.16	11.30	18.97	35.30	11.29	35.55
	–	–	–	–	–	–	-4.17	10.28	1.86	-3.82	10.44	5.31
HD 36444	7.27	11.16	12.03	6.91	11.28	7.96	9.02	11.44	25.95	8.79	11.30	36.31
	21.96	11.70	38.88	21.72	11.82	27.16	22.13	11.95	72.57	22.15	11.87	109.98
	31.40	11.11	10.57	31.98	11.13	5.79	30.81	11.23	16.26	31.00	10.98	18.06
	38.79	11.21	13.46	42.23	11.33	9.06	–	–	–	–	–	–
HD 290609	-9.23	10.91	6.86	–	–	–	-8.56	10.43	2.61	–	–	–
	9.65	11.98	71.21	9.35	12.04	44.61	8.46	11.62	38.92	8.50	11.54	61.20
	24.00	12.01	69.05	24.08	12.06	43.66	22.92	12.26	125.13	23.02	12.08	149.96
	34.38	11.62	33.45	37.31	11.85	29.57	35.39	11.33	20.65	32.52	11.12	24.87
	49.65	11.63	35.35	55.24	11.63	17.92	53.69	10.78	5.84	46.45	10.75	11.01
HR 1919	10.92	11.20	12.71	10.56	11.11	5.48	10.39	10.44	2.71	10.63	10.36	4.44
	32.17	11.57	28.28	30.84	11.37	9.74	30.92	10.46	2.80	30.51	10.34	4.27
	38.79	10.64	3.66	35.43	11.12	5.61	36.77	9.69	0.48	35.58	9.97	1.82
HD 54341	10.32	10.07	1.01	–	–	–	–	–	–	–	–	–
	24.49	10.36	1.96	26.17	10.50	1.35	24.95	9.91	0.79	25.91	10.05	2.22
	–	–	–	–	–	–	–	–	–	3.31	9.85	1.39
HD 60856	20.39	11.69	36.77	20.14	11.82	26.63	20.38	12.25	118.41	20.38	12.03	134.94
	30.65	10.71	4.37	31.10	10.82	2.85	28.72	10.70	4.86	29.47	10.42	5.13
HR 3300	5.62	10.77	4.99	4.95	10.50	1.38	7.52	10.18	1.49	5.72	10.19	3.01
	15.83	10.21	1.37	16.04	10.28	0.83	17.66	10.20	1.57	17.45	10.22	3.27
	20.82	10.30	1.69	–	–	–	–	–	–	–	–	–
η Cha	-3.37	10.13	1.16	-3.46	10.11	0.55	-1.05	9.57	0.36	-3.46	9.84	1.36
	10.09	10.77	4.97	9.55	10.76	2.49	11.92	10.46	2.85	12.20	10.44	5.34
HD 92536	2.81	10.60	3.36	1.57	10.22	0.72	-0.23	9.50	0.31	-0.56	9.74	1.07
	9.94	11.40	19.84	9.59	11.45	11.85	9.19	11.55	31.90	9.18	11.53	56.67
	18.21	11.27	15.18	18.31	11.22	6.96	17.59	10.90	7.77	17.25	10.90	15.15
3 Crv	-6.64	11.05	9.23	-7.69	10.83	2.89	-6.81	10.76	5.53	-6.86	10.71	9.60
	-1.45	10.67	3.86	-3.19	11.01	4.35	-1.22	9.83	0.67	-1.71	9.91	1.60
	2.21	10.54	2.95	3.70	9.69	0.21	–	–	–	–	–	–
HD 106036	-6.17	11.03	9.13	-3.40	11.20	6.78	–	–	–	–	–	–
	9.97	11.30	16.57	10.39	11.08	5.13	–	–	–	–	–	–
HR 4796	-14.40	10.41	2.18	-14.60	10.49	1.33	-11.10	9.89	0.76	-11.76	9.85	1.40
	-5.57	10.40	2.14	-5.84	10.26	0.79	-5.01	10.51	3.19	-5.11	10.54	6.75
	5.20	9.78	0.52	–	–	–	–	–	–	–	–	–
HD 110058	1.85	11.47	24.38	0.97	11.45	12.04	0.56	11.23	16.31	0.42	11.24	32.67
	12.50	11.50	21.89	12.19	11.77	20.79	12.36	11.76	41.72	12.34	11.49	43.52

Continued on next page

Table 6 – continued from previous page

Name	CaII K			CaII H			NaI D1			NaI D2		
	radV [km.s ⁻¹]	log ₁₀ <i>N</i> [cm ⁻²]	<i>EW</i> [mÅ]	radV [km.s ⁻¹]	log ₁₀ <i>N</i> [cm ⁻²]	<i>EW</i> [mÅ]	radV [km.s ⁻¹]	log ₁₀ <i>N</i> [cm ⁻²]	<i>EW</i> [mÅ]	radV [km.s ⁻¹]	log ₁₀ <i>N</i> [cm ⁻²]	<i>EW</i> [mÅ]
HD 112810	-12.11	11.07	9.76	-10.86	10.88	3.23	–	–	–	–	–	–
	-3.76	11.60	29.69	-4.49	11.57	14.99	–	–	–	–	–	–
	3.77	11.01	8.46	2.28	11.25	7.58	–	–	–	–	–	–
HD 126135	-22.78	10.25	1.51	–	–	–	-22.49	10.01	1.01	-22.12	10.06	2.23
	-14.89	10.73	4.45	-15.59	10.60	1.71	-13.47	10.84	6.73	-14.36	10.67	9.03
	-8.32	10.59	3.27	-9.90	10.56	1.57	-7.83	10.02	1.04	-10.23	10.46	5.64
	4.16	10.92	6.83	3.83	10.85	3.05	4.25	11.59	33.50	4.36	11.57	58.21
HD 141378	–	–	–	–	–	–	–	–	–	26.30	9.63	0.84
	-30.03	10.79	5.16	–	–	–	–	–	–	–	–	–
HD 141327	-15.02	10.36	1.93	–	–	–	–	–	–	–	–	–
	-18.37	11.33	18.11	-21.23	11.22	7.07	-23.48	10.42	2.58	-23.69	10.41	4.97
HR 6507	-1.43	11.95	66.92	-2.40	11.97	37.57	-4.17	12.51	203.27	-4.20	12.43	260.97
	14.78	11.80	47.59	14.23	11.82	26.94	14.66	10.77	5.73	14.16	10.77	11.18
	22.92	11.04	9.25	21.83	10.97	4.06	23.11	10.60	3.90	22.75	10.75	10.90
	-38.93	10.32	1.78	-39.26	11.02	4.49	-38.62	10.39	2.40	-39.01	9.97	1.82
	-30.41	11.12	10.98	-29.52	11.29	8.22	-29.80	10.26	1.80	-29.10	10.42	5.09
c Aql	-24.86	11.25	14.00	-25.05	11.22	6.84	-25.08	10.97	8.71	-25.09	10.91	14.68
	-31.19	10.49	2.64	-31.67	10.52	1.44	–	–	–	–	–	–
	-19.67	10.34	1.88	-19.88	10.44	1.21	–	–	–	–	–	–

4.5 Variability of the extra absorption features

We investigated the variability of additional absorption lines in two ways: first by analysing their stability when they are detected in all the epochs and second by looking for transient absorption features that appear in a handful of epochs. For the first method, we performed the same Gaussian fitting described above, but on each individual epoch and we searched for variations in flux and velocity of those “stable” components (since they are present in all the epochs they also appear in the reference spectrum). For the second method, we searched for additional variable detections above a 3σ level that might appear in some of the epochs. Such transient detections could be related to FEB-like events.

We found variable absorption features attributable to FEB-like events in specific epochs of the objects c Aql and HR 4796. In particular, in the case of c Aql we detected very short-term variations from within a few nights to within a few minutes. Variations detected on the night of 2011-05-27 are shown in Fig. 3 for the Ca II K line, and they are also present in the Ca II H and Na I lines for some of the observations. These variations, likely attributable to intense exocometary activity, are detected at $\sim 35 \text{ km.s}^{-1}$, red-shifted with respect to the radial velocity of the star.

We have also detected variability in the Ca II K line of HR 4796. The observed variations appear as a small feature detected at 5.30 km.s^{-1} , matching the radial velocity of the star (5.35 km.s^{-1}). Since we have collected over 200 individual spectra of HR 4796, in Fig. 3 we only show a selection of a few epochs as examples of the variability observed around this star. These detections are narrow and only slightly over 3σ . Since the strength of Ca II H line is roughly half that of the Ca II K line, we do not expect to have a significant detection in the latter (as was the case). However, it is reassuring (in the circumstellar gas scenario) that all the detections in the Ca II K line match the radial velocity of the star.

In addition, we have detected low-level ($\sim 2\sigma$) variability in the residual spectra of HR 6507. However, this variability presents itself as a very broad component covering the full range of velocities of the photospheric line, as can be seen in Fig. 4. In order to determine if this variability was produced by circumstellar gas or the star itself, we also analysed the H_α line. Neither narrow emission nor absorption were detected in this line. However, the same broad variability was found, more consistent with photospheric variation. This star is classified as a shell star in (Hauck & Jaschek 2000, Jaschek et al. 1991), but even the shell classification is questioned in Jaschek et al. (1988) and Jaschek & Andrillat (1998). From the velocity field involved, this variability is more likely due to the presence of spots (as described in Figueira 2013).

4.6 Local Interstellar Medium features

4.6.1 Objects with known clouds in the line of sight

We looked for local interstellar clouds in the line of sight of the stars, as this clouds could explain the presence of the extra absorption lines that we observe. We used the on-line Local InterStellar Medium (LISM) Kinematic Calculator⁸ (Redfield & Linsky 2008) which predicts the radial and transverse velocities of LISM clouds in any direction and calculates which clouds are traversed by any given line of sight.

We found traversing known clouds from the Redfield & Linsky (2008) catalogue for 18 of our objects and, in most cases, the radial velocity of the clouds matched the velocity of some of the absorption features. In Table 8 we present the clouds traversing the line of sight of each object, their heliocentric radial velocities and whether they match one of the absorption lines or not. As can be seen in the Table, a significant number of our features are attributable to gas located in the G cloud, which is an interstellar cloud located next to the Local Interstellar Cloud (LIC).

4.6.2 Objects with Diffuse Interstellar Bands

We have analysed the Diffuse Interstellar Bands (DIBs) at wavelengths 5780.5\AA and 5797.1\AA . DIBs are absorption features caused by the ISM and they can be detected in the UV, optical and IR wavelengths. DIBs are much broader than the atomic interstellar lines, having full width at half maximum ranging from $\sim 0.8\text{-}30 \text{\AA}$, presumably due to unresolved rotational structure of large carbon-bearing molecules, which are common in the interstellar medium (Herbig 1995). The DIBs we have chosen to analyse are some of the strongest DIBs detectable in optical spectra. The presence of absorption features at any of these particular wavelengths might indicate the presence of ISM in the line of sight of the star, as DIBs are hardly attributable to circumstellar gas around pre-main sequence or main sequence stars (as opposed to objects that have departed the main sequence, see for e.g. Díaz-Luis et al. 2015).

We detected the presence of absorption lines likely to be due to DIBs in the 12 objects listed in Table 7. These absorption lines are broad and diffuse, making it difficult to obtain precise measurements of their radial velocities. Therefore we use this criteria mostly to confirm the presence of ISM within a certain velocity range. We note that although in most cases we have identified diffuse bands at both wavelength locations, for HR 3300, HD 92536, and HD 126135 we have detected DIBs at only one of the wavelengths. This can be explained by the fact that the intensity of the bands detected for those three sources is much lower than in the other cases; therefore we interpret the difference as a sensitivity issue rather than a physical one.

⁸ <http://lism.wesleyan.edu/LISMdynamics.html>

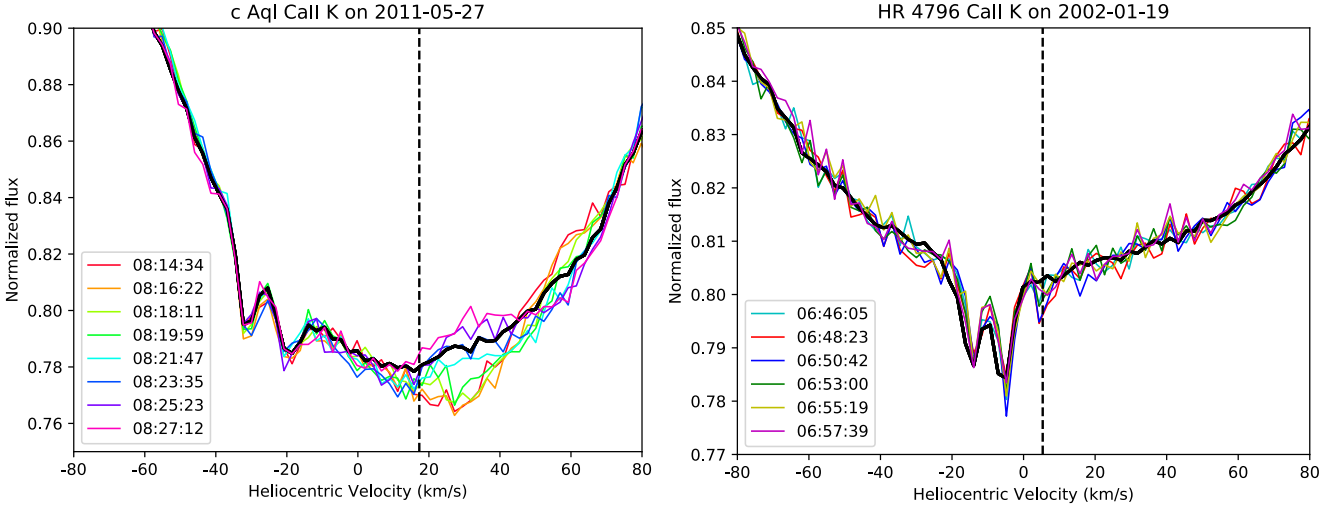


Figure 3. Left: Variability in the Ca II K line of c Aql during the night of 2011-05-27, the UT of each observation is shown in the legend. Right: Example of variability detected in HR 4796 at the stellar radial velocity along a selection of spectra taken on 2002-01-19. The thick black line in each Figure shows the median spectrum for comparison. The radial velocity of the star is marked with a dashed black line in both Figures.

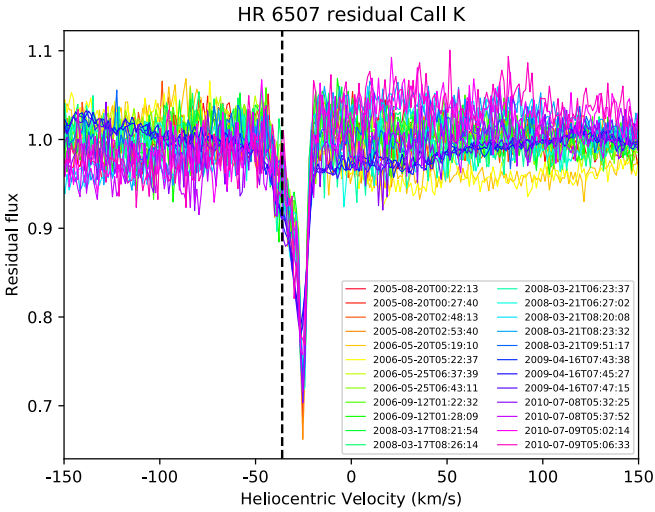


Figure 4. Variability in the residuals of the Ca II K line of HR 6507 after normalizing all the epochs by the reference spectrum. The date of each observation is shown. The radial velocity of the star is marked with a dashed black line.

4.6.3 Nearby stars analysis

Similarly to the analysis performed on the objects in our sample, we analysed the Ca II K lines of nearby stars searching for the presence of absorption features at similar velocities to the ones observed in our objects. Finding these similar absorption lines in the line of sight towards nearby stars would strongly suggest an ISM origin for the gas feature(s). We chose to analyse the Ca II K line since its absorption is more intense and easier to detect than the H line and it is the main tracer of circumstellar gas in the optical.

For each star of our sample, we searched for high resolution spectra of nearby stars within a search-box of up to

Table 7. Summary of the detection of absorptions consistent with DIBs at either 5780.5Å or 5797.1Å.

Name	DIB at 5780.5 Å	DIB at 5797.1 Å
β 03 Tuc	✗	✗
66 Psc	✗	✗
ν Hor	✗	✗
HD 24966	✗	✗
HD 290540	✓	✓
HD 36444	✓	✓
HD 290609	✓	✓
HR 1919	✗	✗
HD 54341	✗	✗
HD 60856	✓	✓
HR 3300	✗	✓
η Cha	✗	✗
HD 92536	✓	✗
3 Crv	✗	✗
HD 106036	✗	✗
HR 4796	✗	✗
HD 110058	✗	✗
HD 112810	✗	✗
HD 126135	✓	✗
HD 141378	✗	✗
HD 141327	✓	✓
HR 6507	✗	✗
c Aql	✗	✗

6 degrees (~ 3 degrees radius). Considering the distances of the objects, the equivalent projected separations between the targets and their neighbours range between ~ 0.1 pc and ~ 30 pc. From the gathered data, we only considered objects having early spectral types, ideally between B0 and F5, since absorption features are harder to detect in later spectral types. Non-photospheric gas absorptions are easily spotted when superimposed on fast rotators having wider (and fewer) spectral lines.

We found suitable nearby stars for all the candidates except for 66 Psc and HD 24966. The observations used for this analysis are described in Table C1. We found absorption

features present in all the nearby stars and they match most of the absorption features found in our objects, confirming the interstellar origin for the majority of the features. In the case of HD 110058, we found that three nearby stars presented one absorption feature matching HD 110058 absorption line at $\sim 1 \text{ km.s}^{-1}$, one star shows a weak absorption matching the radial velocity of the G cloud, but none of the nearby stars shows any signs of absorption lines matching the one at $\sim 12 \text{ km.s}^{-1}$, which also happens to be near the estimated radial velocity of this star. Therefore we propose a circumstellar origin for this feature.

A comparison of the nearby stars absorption lines against our objects and their respective angular separations are shown in Figs. C1 to C4.

4.7 General results

We present a summary of our results regarding stable features in Table 8, in which we report the radial velocity of the star, the traversing clouds, their radial velocities and whether they match one of the observed features, the average velocities of each absorption feature, its CaII/NaI density ratio, whether it has a matching absorption in a nearby star and our verdict on its origin; ISM (InterStellar Medium) or CS (CircumStellar).

Most of the stable features are likely produced by clouds in the line of sight and not by the circumstellar medium, except in the cases of HR 4796 and HD 110058. We find that two objects present variability: HR 4796 shows flux variations in its feature located at the same velocity as the star and ϵ Aql exhibits transient red-shifted absorption lines with characteristics of FEB-like events. Another interesting case is that of HR 6507, for which a clear diagnostic cannot be attained with the available data as discussed in Sec. 5.2.2.

Table 8: Absorption components and their mean radial velocity, CaII/Nai density ratio, absorption feature detection in a nearby star and proposed origin.

Name	Stellar RV [km.s ⁻¹]	Cloud Name	Cloud RV [km.s ⁻¹]	Matching Feature?	Feature RV [km.s ⁻¹]	$\frac{N(\text{CaII})}{N(\text{NaI})}$	Nearby star	Origin
β 03 Tuc	6.05 ± 1.60	–	–	–	-11.22	3.47	✓	ISM
		Dor	13.85 ± 0.65	✗	-3.74	0.38	✓	ISM
		Vel	2.54 ± 0.78	✓	2.26	13.08	✓	ISM
66 Psc	4.32 ± 2.66	–	–	–	-5.71	0.63	–	ISM
		–	–	–	0.49	0.40	–	ISM
ν Hor	13.58 ± 1.67	LIC	11.44 ± 1.29	✓	11.49	7.03	–	ISM
		G	5.33 ± 1.52	✓	4.11	6.16	✓	ISM
		Vel	12.65 ± 0.93	✓	12.74	2.94	✓	ISM
HD 24966	15.70 ± 3.15	Cet	9.85 ± 0.63	✗	-9.09	< 1	✓	ISM
		Blue	10.59 ± 1.30	✗	-13.10	> 5	–	ISM
		G	17.51 ± 1.38	✓	15.68	8.40	–	ISM
HD 290540	27.26 ± 3.12	Dor	32.11 ± 0.85	✓	32.15	6.58	–	ISM
		–	–	–	9.28	1.31	✓	ISM
		–	–	–	23.78	1.04	✓	ISM
HD 36444	26.72 ± 4.50	–	–	–	35.51	0.46	✓	ISM
		–	–	–	-3.99	< 1	✓	ISM
		LIC	22.75 ± 0.96	✓	8.00	0.70	✓	ISM
HD 290609	25.87 ± 1.65	–	–	–	21.99	0.72	✓	ISM
		–	–	–	31.30	1.00	✓	ISM
		–	–	–	40.51	> 5	✓	ISM
HR 1919	23.49 ± 1.28	–	–	–	-8.89	3.05	✓	ISM
		–	–	–	8.99	2.70	✓	ISM
		–	–	–	23.50	0.73	✓	ISM
HD 54341	41.03 ± 0.95	–	–	–	34.90	3.24	✓	ISM
		–	–	–	51.26	7.33	✓	ISM
		–	–	–	10.63	5.59	✓	ISM
HD 60856	31.89 ± 1.59	–	–	–	31.11	11.97	✓	ISM
		–	–	–	36.64	12.35	✓	ISM
		Blue	9.59 ± 0.93	✓	3.31	< 1	✓	ISM
HR 3300	22.35 ± 0.72	–	–	–	10.32	> 5	✓	ISM
		LIC	16.37 ± 1.18	✗	25.38	2.80	✓	ISM
		–	–	–	20.32	0.40	✓	ISM
η Cha	15.21 ± 1.41	–	–	–	29.98	1.55	✓	ISM
		G	4.62 ± 0.94	✓	5.95	2.97	✓	ISM
		Vel	15.00 ± 0.97	✓	16.75	1.08	✓	ISM
HD 92536	15.45 ± 0.44	Cet	20.50 ± 0.87	✓	20.82	> 5	✓	ISM
		G	-4.07 ± 1.17	✓	-2.84	2.47	✓	ISM
		Vel	0.02 ± 0.75	✗	10.94	2.07	✓	ISM
3 Crv	14.41 ± 1.09	G	-6.09 ± 0.97	✗	0.90	6.52	✓	ISM
		–	–	–	9.47	0.77	✓	ISM
		–	–	–	17.84	2.21	✓	ISM
HD 106036	9.37 ± 2.34	Leo	-5.36 ± 1.05	✓	-7.00	1.65	✓	ISM
		–	–	–	-1.89	9.91	✓	ISM
		Gem	2.54 ± 0.95	✓	2.96	> 5	✓	ISM
HR 4796	5.35 ± 2.94	G	-11.13 ± 0.98	✗	-4.78	–	✓	ISM
		–	–	–	10.18	–	✓	ISM
		–	–	–	-12.97	3.79	✓	ISM
HD 110058	11.20 ± 0.81	–	–	–	-5.38	0.64	✓	ISM
		G	-14.46 ± 0.97	✗	5.20	> 5	✗	CS
		–	–	–	0.95	1.68	✓	ISM
HD 112810	5.25 ± 2.24	–	–	–	12.35	1.02	✗	CS
		G	-15.70 ± 0.97	✗	-11.48	–	✓	ISM
		–	–	–	-4.12	–	✓	ISM
HD 126135	11.73 ± 0.67	–	–	–	3.02	–	✓	ISM
		NGP	-24.28 ± 1.22	✓	-22.46	0.82	✓	ISM

Continued on next page

Table 8 – continued from previous page

Name	Stellar RV [km.s ⁻¹]	Cloud Name	Cloud RV [km.s ⁻¹]	Matching Feature?	Feature RV [km.s ⁻¹]	$\frac{N(\text{CaII})}{N(\text{NaI})}$	Nearby star	Origin
		Gem	-14.33 ± 1.01	✓	-14.58	0.80	✓	ISM
		–	–	–	-9.07	1.89	✓	ISM
		–	–	–	4.15	0.20	✓	ISM
		–	–	–	26.30	< 1	✓	ISM
HD 141378	-14.68 ± 2.62	G	-28.37 ± 1.18	✓	-30.03	> 5	✓	ISM
		–	–	–	-15.02	> 5	✓	ISM
HD 141327	-4.65 ± 2.40	G	-27.31 ± 1.08	✗	-21.69	7.32	✓	ISM
		–	–	–	-3.05	0.31	✓	ISM
		–	–	–	14.46	11.08	✓	ISM
		–	–	–	22.65	2.12	✓	ISM
HR 6507	-36.13 ± 2.49	–	–	–	-38.95	3.72	✓	ISM
		–	–	–	-29.71	7.33	✓	ISM
		–	–	–	-25.02	1.99	✓	ISM
c Aql	17.29 ± 2.61	Mic, Aql	-26.86, -25.26	✗	-31.43	> 5	✗	ISM
		Eri	-20.11 ± 1.14	✓	-19.77	> 5	✓	ISM

5 DISCUSSION

Gas absorption features superimposed on photospheric lines look fairly similar whether they are caused by clouds in the line of sight of the star or by the presence of stable gas in the circumstellar environment. Therefore, a detailed analysis, involving multiple criteria, has to be performed in order to discriminate between the two scenarios. Below we discuss our results regarding the origin of the features in “interstellar” and “circumstellar” categories.

5.1 Interstellar-like features

Most of the absorption features found in this study are classified as “interstellar” as they do not present significant time variability beyond the noise level or attributable to different instrument or resolution. In addition, all these features possess other characteristics such as having a composition consistent with typical ISM values, matching clouds in their line of sight, or detection of a similar feature in a nearby star with velocities matching within 3σ .

Overall, we found 21 absorption features matching the radial velocity of known clouds traversing the lines of sight of the stars. A summary of the traversing clouds, their radial velocities and the matching absorptions is provided in Table 8. The evidence for these features to be caused by those clouds in the line of sight, is strengthened by the fact that they are also detected in nearby stars around our science targets. A particular case of this phenomenon is observed in the objects HD 290540, HD 36444 and HD 290609.

These three stars are located within an angular separation of 0.7° of each other. As can be seen in Fig. C1, the three objects present similar absorption features at similar velocities, which are also detected for three other nearby stars within an angular radius of 1° . We obtained comparable radial velocities for these three objects, around 26 km.s^{-1} . As noticeable in Fig. C1, they all have a deep absorption line close to 23 km.s^{-1} , which corresponds to the Local Interstellar Cloud (LIC, Redfield & Linsky 2008). Although this absorption line is found to be close to the radial velocity of the stars, its interstellar origin is clear as it is confirmed by being present in other three stars with a similar line of sight and having a $N(\text{CaII}/\text{NaI})$ ratio consistent with ISM ($\lesssim 1$). The other absorption lines seen in the three objects at ~ 9 and $\sim 34 \text{ km.s}^{-1}$ also seem to have a common interstellar origin. The one at $\sim 9 \text{ km.s}^{-1}$ is possibly attributable to the Hyades cloud at $\sim 11 \text{ km.s}^{-1}$, which according to Redfield & Linsky (2008) crosses near ($< 20^\circ$) the line of sight of these three stars. We did not find any known cloud traversing a similar line of sight at a radial velocity close to $\sim 34 \text{ km.s}^{-1}$, however, since this absorption line is present in several stars at a similar velocity we also conclude that it is of interstellar origin.

There is a fourth feature at $\sim 41 \text{ km.s}^{-1}$ for HD 36444 detected only in the CaII lines which, due to its mostly Calcium composition ($N(\text{CaII}/\text{NaI}) > 5$) could be consistent with having a circumstellar origin. However, a similar fea-

ture is observed in the nearby star HR 1863, and therefore it is likely to be another feature of interstellar origin, possibly warm ISM, which has been reported to have a composition richer in Calcium than cold ISM (Bertin et al. 1993). Unfortunately we have obtained only one epoch for HD 36444 therefore we were not able to investigate the variability of this feature. Further data is thus necessary in order to fully rule out circumstellar origin.

HD 290609 also presents a fourth feature, but it is detected around $\sim 51 \text{ km.s}^{-1}$. However, we point out that this group of stars is located within the Orion OB1 association (Hernández et al. 2006) making it likely that environmental nebular gas is observed at different velocities (Brown et al. 1994). In any case, although we conclude an ISM origin for HD 290609’s fourth feature because of the high frequency of interstellar clouds observed in the surroundings; as in the previous case, there is only one spectrum available for HD 290609 and it would be interesting to perform further analysis gathering more epochs in order to better assess the origin of this feature.

5.2 Circumstellar-like features

5.2.1 Stable features with no matching absorptions in nearby stars

In the case of HD 110058, we found that three nearby stars present one absorption feature matching HD 110058’s absorption at $\sim 1 \text{ km.s}^{-1}$, thus we propose an interstellar origin for this feature. This interstellar feature was also reported by Hales et al. (2017), who analysed MIKE spectra of HD 110058 and three nearby stars (at angular separations between 1.2° and 2.8°) and found matching features for the absorption at $\sim 1 \text{ km.s}^{-1}$. We obtained further spectra for four different nearby stars in the ESO archive (at angular separations between 0.74° and 2.16°) and confirmed the matching absorption lines in three stars, in agreement with the findings by Hales et al. (2017). Given the distance to this star ($188.7 \pm 34.1 \text{ pc}$), both studies cover a region of $2.4 - 9.2 \text{ pc}$ in radius. Considering a typical radius of 1.5 pc for the warm local ISM material located within 15 pc from the Sun (Redfield & Linsky 2008), the projected coverage at the distance of HD 110058 would be about 19 pc , thus the local ISM material would likely cover the region in which the nearby stars are located. On the other hand, our measurements of the equivalent widths of this feature is in agreement with a more recent work by Rebollido et al. (2018), where the authors report that the strength measured for this blue-shifted component varies with respect to Hales et al. (2017) measurement, proposing a possible circumstellar origin for the blue-shifted feature at $\sim 1 \text{ km.s}^{-1}$. Considering the scenario of variability in the blue-shifted component and a possible overlap of circumstellar feature over the interstellar it would be worth performing follow-up observations of this object to better assess the origin of this feature. There is a fourth nearby star analyzed which does not present a feature at said velocity, but shows a weak absorption line at $\sim -15 \text{ km.s}^{-1}$ matching the radial velocity of the G cloud. HD 110058 presents an additional absorption feature at \sim

12 km.s^{-1} which is very near our estimate of the radial velocity of this star (11.20 km.s^{-1}). None of the nearby stars analyzed show any sign of absorption matching HD 110058's absorption line at $\sim 12 \text{ km.s}^{-1}$. Therefore we propose a circumstellar origin for this feature. This circumstellar feature was also proposed by [Hales et al. \(2017\)](#) and confirmed by [Rebollido et al. \(2018\)](#), thus our analysis is in agreement with their conclusions.

5.2.2 Variable features

We detected variable absorption features attributable to FEB-like events in the objects cAql and HR 4796. The detection of FEB-like events in cAql was previously reported by [Montgomery & Welsh \(2017\)](#), where they detected high variations from night to night and attributed them to exocometary activity. Furthermore [Welsh & Montgomery \(2013\)](#) reported some nightly changes but no FEBs-like events. With the data collected from the ESO archive we found, in addition to night to night variations, strong variability within very short time scales of only a couple of minutes. To our knowledge, this is the shortest-term variability detected to date in such systems. This object is known to be a pulsating star with a period of 30.39 minutes ([Kuschnig et al. 1994](#)) but a phase analysis of the CaII K and the H α lines does not indicate any such periodicity. In addition, the residual absorption events are not associated with a counterpart in emission at a mirrored velocity with respect to the radial velocity of the star (even taking into account the uncertainty in the latter), as one would expect from pulsations. In the left panel of Fig. 3, we show the variability detected in cAql through eight individual spectra taken within a time span of ~ 20 minutes. Similar short term variability has only been observed so far in β Pictoris ([Kiefer et al. 2014b](#)) and the shell star ϕ Leo ([Eiroa et al. 2016](#)), with reported variability within hours.

Variability in the CaII K line of HR 4796 at the same radial velocity of the star is reported here for the first time. Previously, only a sporadic absorption at $\sim 60 \text{ km.s}^{-1}$ during the night of 2007-05-04 was reported by [Welsh & Montgomery \(2015\)](#). A more detailed analysis of the variability detected in these two objects will be presented in [Iglesias et al. \(in prep\)](#).

Regarding other objects in our sample with claims of variability in the literature, there are also HR 6507 ([Welsh & Montgomery 2015](#)) and HD 24966 ([Welsh & Montgomery 2018](#)). In the case of HR 6507, [Welsh & Montgomery \(2015\)](#) modelled the absorption lines using two components at radial velocities $\sim -37 \text{ km.s}^{-1}$ and $\sim -28 \text{ km.s}^{-1}$. The observations were taken with the Sandiford Echelle Spectrograph at the McDonald Observatory, Texas, with ~ 60000 resolution. We combined HARPS and UVES spectra (with higher resolution, ~ 100000 and ~ 80000 , respectively) and were able to distinguish and fit three absorption features at radial velocities $\sim -39 \text{ km.s}^{-1}$, $\sim -29 \text{ km.s}^{-1}$ and $\sim -25 \text{ km.s}^{-1}$. [Welsh & Montgomery \(2015\)](#) attributed a circumstellar origin for the feature observed at $\sim -37 \text{ km.s}^{-1}$ because of its proximity to the radial velocity of the star ($\sim -36 \text{ km.s}^{-1}$).

However, for the corresponding feature, which we measure at $\sim -39 \text{ km.s}^{-1}$, we found absorption lines of similar velocity and intensity in nearby stars, suggesting ISM origin.

HR 6507 has also been reported to possess shell star signatures ([Hauck & Jaschek 2000](#), [Jaschek et al. 1991](#)), although in other works no clear indication of a shell has been found, attributing this to a weakening or disappearing of the shell ([Jaschek et al. 1988](#), [Jaschek & Andriolat 1998](#)). Nevertheless, considering the possibility of HR 6507 being a shell star, it is likely that it possesses circumstellar gas and therefore shows gas signatures at its radial velocity. As mentioned in 4.5, we found small variability in the overall residuals of all the lines observed for HR 6507. In [Hauck & Jaschek \(2000\)](#), they report the star as variable and possibly micro-variable, which might explain the observed variations. Taking all this into account, we do not attribute the variability to FEBs-like events, but a more detailed study of this source is needed to achieve stronger conclusions.

In the case of HD 24966, [Welsh & Montgomery \(2018\)](#) recently proposed the detection of exocomets at different velocity ranges in two out of three observations. The significance and interpretation of such variable transient FEB absorption features will be further investigated in [Iglesias et al. \(in prep\)](#).

5.2.3 Relationship between circumstellar-like features and system properties

Gas absorptions features of presumed circumstellar origin were found in the systems HD 110058, HR 4796 and cAql.

The debris disk around HD 110058 has been resolved with SPHERE by [Kasper et al. \(2015\)](#), where they determined an inclination of $\sim 90^\circ$. This edge-on orientation reinforces the circumstellar verdict on the gas origin, as this is the most favourable orientation for potentially detecting gas lines in absorption. Since the absorption line that we detect is deep, narrow, stable, and close to the radial velocity of the star, it is consistent with a stable gas component, possibly located in the outer regions of the disk ([Beust et al. 1998](#), [Brandeker et al. 2004](#)).

HR 4796 has an inclination of 76.5° ([Milli et al. 2017](#), [Kennedy et al. 2018](#)) which is fairly close to edge-on. Since somewhat small misalignments in cometary orbits with respect to the parental disk are common ([Nesvorný et al. 2017](#)), it is not necessarily unlikely to detect FEB events.

Regarding the disk around cAql, it has only been marginally resolved with Herschel by [Morales et al. \(2016\)](#). They estimated an inclination of $21^\circ \pm 42^\circ$. Although this inclination does not seem favourable for circumstellar gas detections using optical spectroscopy, the estimated uncertainty on the inclination is very large as the disk was only marginally resolved. The possibility of a much higher inclination cannot be ruled out. Even if the shallower inclination is confirmed, we could still be spotting the activity of bodies with highly inclined orbits. Overall, it is reassuring that two

of our candidates with gas detections are close to edge-on, with very robust inclination determinations.

Regarding the rest of the sample, only two other objects have been marginally resolved (with Herschel): ν Hor, modelled with $73.4^\circ \pm 6.5^\circ$ inclination (Moór et al. 2015), and HD 141378, with an estimated inclination of $60^\circ \pm 37^\circ$ (Morales et al. 2016). We did not detect signs of circumstellar gas in these objects. Nevertheless, it would be worth performing follow-up studies to be able to analyse more epochs and therefore increase the chances of detecting stochastic activity or provide more robust evidence of the lack of such activity.

6 CONCLUSIONS

In this work we have analysed the multiple absorption features present in the Ca II H & K and Na I D1 and D2 lines of 23 debris disks systems using optical high-resolution spectroscopy in order to determine if their origin is of circumstellar or interstellar nature.

We found gas absorptions of circumstellar nature in three objects: HD 110058, HR 4796 and c Aql. HD 110058 presents a strong stable absorption consistent with a gaseous disk, possibly residual gas leftover from the earlier gas-rich stage of the disk or from very active planetesimal collision episodes.

Variable absorption features were found in the spectra of HR 4796 and c Aql. A weak circumstellar absorption was found in HR 4796 at the same radial velocity as the star with flux variations over 3σ , possibly due to photo-dissociation processes or collisions of icy bodies producing changes in the gas content of the disk. Highly variable red-shifted absorptions were detected in c Aql, with substantial variations observed on time scales shorter than two minutes, which is the shortest variability detected so far in this type of lines. These fast changing signatures are likely due to exocometary activity within the disk surrounding c Aql. For these two objects, HR 4796 and c Aql, we will present a more detailed analysis of the variable features in a future work. The circumstellar gas detections are in agreement with the near edge-on inclinations of the two objects with robust inclination measurements: HD 110058 with an inclination of $\sim 90^\circ$ and HR 4796 with an inclination of 76.5° .

Given h , r and i the scale-height, radial distance and inclination of a circumstellar disk, respectively, and assuming a typical scale-height/distance ratio of $h/r \sim 0.1$ for debris disks (Thébaud 2009), the typical angle subtended by the disk should be $\sim 5.7^\circ$. For a uniform distribution of $\sin(i)$ between 0 and 1, the probability of $i \geq (90^\circ - 5.7^\circ)$ is $\sim 10\%$, and therefore, the probability for a randomly inclined system to be found close to edge-on or with an inclination suitable to detect circumstellar gas absorptions is $\sim 10\%$.

However, the sample analyzed in this paper cannot, a priori, be considered “random” because of the selection criterion of “having multiple absorption features” (that may

bias the sample towards objects with circumstellar gas on close to edge-on orientation). On the other hand, this sample is actually unbiased with respect to stochastic detections such as FEBs (we remind the reader that the selection function was performed on the reference spectra, i.e. only stable components are considered).

Bearing in mind that the inclination constraints could be more relaxed regarding the detection of FEBs (as discussed in Sec. 5.2.3); that FEBs, given their stochastic nature, may not be detected by mere chance at our epochs of observations; and that, in any case, we do detect circumstellar gas in three cases out of 23 objects (one stable and two variables); our results definitely point towards gas in debris disks not being a rare phenomenon. We will, however, have more quantitative and robust results on this matter once the full sample of 301 debris disks is analyzed.

ACKNOWLEDGEMENTS

DI would like to thank Iván Lacerna, support astronomer at the MPG/ESO 2.2m telescope, La Silla Observatory, for his significant help and support during the observing runs with FEROS and Alain Smette, the author of Molecfit, for his great help on improving telluric corrections. AB and DI acknowledge financial support from the Proyecto Fondecyt Iniciación 11140572. DI, AB and JO acknowledge support from the Millennium Science Initiative (Chilean Ministry of Economy), through grant Núcleo Milenio de Formación Planetaria. This work has made use of data from the ESA space mission Gaia (<http://www.cosmos.esa.int/gaia>), processed by the Gaia Data Processing and Analysis Consortium (DPAC, <http://www.cosmos.esa.int/web/gaia/dpac/consortium>). Funding for the DPAC has been provided by national institutions, in particular the institutions participating in the Gaia Multilateral Agreement. This publication makes use of VOSA, developed under the Spanish Virtual Observatory project supported from the Spanish MICINN through grant AyA2011-24052. Data from the following programmes have been used in this work: CNTAC 096.A-9018(A) and 094.A-9012(A); and ESO 096.C-0238(A), 097.C-0409(A), 097.C-0409(B), 073.C-0733(E), 075.C-0689(A), 077.C-0295(A), 077.C-0295(B), 184.C-0815(A), 184.C-0815(E), 184.C-0815(F), 096.C-0238(A), 075.C-0689(B), 077.C-0295(D), 080.C-0712(A), 094.C-0946(A), 076.C-0279(A), 076.C-0279(B), 076.C-0279(C), 078.C-0209(A), 082.A-9004(A), 088.A-9029(A), 66.D-0284(A), 60.A-9036(A), 60.A-9120(B), 60.A-9122(B), 084.A-9003(A), 085.A-9027(G), 184.C-0815(C), 68.C-0548(A), 078.A-9059(A), 079.A-9007(A), 079.A-9009(A), 079.C-0789(A), 085.A-9027(B), 084.D-0067(A), 087.A-9013(A), 092.A-9006(A), 179.C-0197(A), 179.C-0197(C), 082.D-0061(A), 077.C-0295(C), 083.C-0676(A), 079.D-0567(A), 083.A-9014(A), 083.A-9014(B), 087.B-0308(A), 073.C-0733(E), 075.C-0689(A), 077.C-0295(A), 077.C-0295(B), 094.A-9012(A), 179.C-0197(B), 088.C-0498(A), 074.B-0455(A), 266.D-5655(A), 194.C-0833(C), 096.A-9030(A), 096.A-9024(A), 082.C-0831(A), 084.C-1008(A), 084.A-9004(B), 091.D-0414(B), 088.A-9003(A), 072.D-0410(A), 098.C-0463(A),

093.D-0852(A), 094.C-0946(A), 094.A-9012(A), 084.A-9003(A), 086.A-9006(A), 078.D-0549(A), 084.A-9003(A), 073.D-0291(A), 074.D-0300(A), 076.C-0503(A), 077.C-0547(A), 078.D-0080(A), 194.C-0833(A), 086.D-0449(A), 086.D-0449(A), 179.C-0197(D), 090.D-0358(A), 60.A-9700(A), 60.A-9036(A), 60.A-9700(G), 078.D-0080(A), 087.D-0010(A), 083.C-0139(A), 078.D-0080(A), 087.C-0227(C), 088.C-0353(A), 089.C-0006(A), 082.B-0484(A), 084.B-0029(A), 266.D-5655(A), 185.D-0056(A), 185.D-0056(C), 266.D-5655(A), 073.D-0504(A), 075.C-0234(A), 079.C-0170(A), 081.C-0475(A), 097.D-0035(A), 072.D-0021(A), 073.D-0049(A), 082.D-0061(A), 075.C-0637(A), 079.C-0789(A), 083.A-9003(A), 085.A-9027(B), 076.B-0055(A), 077.C-0295(A), 077.C-0295(C), 083.A-9014(A), 083.A-9011(B), 083.A-9014(B), 084.A-9011(B), 085.A-9027(G), 089.D-0097(B), 090.D-0061(B), 091.D-0145(A), 179.C-0197(C), 091.C-0713(A), 075.D-0342(A), 075.C-0689(A), 075.C-0689(B), 077.C-0295(D), 075.C-0689(B), 077.C-0295(D), 077.C-0295(C), 184.C-0815(F), 179.C-0197(A), 077.C-0138(A), 091.D-0122(A), 081.D-2002(A), 293.D-5036(A), and 083.D-0034(A).

REFERENCES

- Alexander R. D., Clarke C. J., Pringle J. E., 2006, *MNRAS*, **369**, 216
- Ballerín N. P., Rieke G. H., Su K. Y. L., Montiel E., 2013, *ApJ*, **775**, 55
- Baraffe I., Chabrier G., Allard F., Hauschildt P. H., 1998, *A&A*, **337**, 403
- Barnes S. I., Tobin W., Pollard K. R., 2000, *Publ. Astron. Soc. Australia*, **17**, 241
- Bayo A., Rodrigo C., Barrado Y Navascués D., Solano E., Gutiérrez R., Morales-Calderón M., Allard F., 2008, *A&A*, **492**, 277
- Bertin P., Lallement R., Ferlet R., Vidal-Madjar A., 1993, *A&A*, **278**, 549
- Beust H., Lagrange A.-M., Crawford I. A., Goudard C., Spyromilio J., Vidal-Madjar A., 1998, *A&A*, **338**, 1015
- Bohlin R. C., Savage B. D., Drake J. F., 1978, *ApJ*, **224**, 132
- Brandeker A., Liseau R., Olofsson G., Fridlund M., 2004, *A&A*, **413**, 681
- Brown A. G. A., de Geus E. J., de Zeeuw P. T., 1994, *A&A*, **289**, 101
- Canovas H., et al., 2017, preprint, ([arXiv:1710.09393](https://arxiv.org/abs/1710.09393))
- Castelli F., Gratton R. G., Kurucz R. L., 1997, *A&A*, **318**, 841
- Chen C. H., Jura M., 2003, *ApJ*, **582**, 443
- Cleeves L. I., Öberg K. I., Wilner D. J., Huang J., Loomis R. A., Andrews S. M., Czekala I., 2016, *ApJ*, **832**, 110
- Dekker H., D’Odorico S., Kaufer A., Delabre B., Kotzłowski H., 2000, in Iye M., Moorwood A. F., eds, *Proc. SPIE Vol. 4008, Optical and IR Telescope Instrumentation and Detectors*. pp 534–545
- Díaz-Luis J. J., García-Hernández D. A., Kameswara Rao N., Machado A., Cataldo F., 2015, *A&A*, **573**, A97
- Docobo J. A., Ling J. F., 2007, *AJ*, **133**, 1209
- Dommanget J., Nys O., 2002, *VizieR Online Data Catalog*, **1274**
- Eiroa C., et al., 2016, *A&A*, **594**, L1
- Fedele D., van den Ancker M. E., Henning T., Jayawardhana R., Oliveira J. M., 2010, *A&A*, **510**, A72
- Fernández R., Brandeker A., Wu Y., 2006, *ApJ*, **643**, 509
- Figueira P., 2013, in Chavez M., Bertone E., Vega O., De la Luz V., eds, *Astronomical Society of the Pacific Conference Series* Vol. 472, *New Quests in Stellar Astrophysics III: A Panchromatic View of Solar-Like Stars, With and Without Planets*. p. 137
- Gaia Collaboration et al., 2016, *A&A*, **595**, A2
- Gontcharov G. A., 2012, *Astronomy Letters*, **38**, 694
- Gray R. O., Corbally J. C., 2009, *Stellar Spectral Classification*
- Greaves J. S., et al., 2016, *MNRAS*, **461**, 3910
- Hales A. S., et al., 2014, *AJ*, **148**, 47
- Hales A. S., Barlow M. J., Crawford I. A., Casassus S., 2017, *MNRAS*, **466**, 3582
- Hauck B., Jäschek C., 2000, *A&A*, **354**, 157
- Herbig G. H., 1995, *ARA&A*, **33**, 19
- Hernández J., Briceño C., Calvet N., Hartmann L., Muzerolle J., Quintero A., 2006, *ApJ*, **652**, 472
- Hernández J., et al., 2007, *ApJ*, **662**, 1067
- Higuchi A. E., et al., 2017, *ApJ*, **839**, L14
- Houck J. R., et al., 2004, *ApJS*, **154**, 18
- Howarth I. D., Price R. J., Crawford I. A., Hawkins I., 2002, *MNRAS*, **335**, 267
- Hughes A. M., Duchene G., Matthews B., 2018, preprint, ([arXiv:1802.04313](https://arxiv.org/abs/1802.04313))
- Jäschek C., Andriillat Y., 1998, *A&AS*, **130**, 507
- Jäschek M., Jäschek C., Andriillat Y., 1988, *A&AS*, **72**, 505
- Jäschek M., Jäschek C., Andriillat Y., 1991, *A&A*, **250**, 127
- Jura M., Zuckerman B., Becklin E. E., Smith R. C., 1993, *ApJ*, **418**, L37
- Kasper M., Apai D., Wagner K., Robberto M., 2015, *ApJ*, **812**, L33
- Kaufer A., Stahl O., Tubbesing S., Nørregaard P., Avila G., Francois P., Pasquini L., Pizzella A., 1999, *The Messenger*, **95**, 8
- Kausch W., et al., 2015, *A&A*, **576**, A78
- Kennedy G. M., Marino S., Matrá L., Panić O., Wilner D., Wyatt M. C., Yelverton B., 2018, *MNRAS*,
- Kenyon S. J., Najita J. R., Bromley B. C., 2016, *ApJ*, **831**, 8
- Kharchenko N. V., 2001, *Kinematika i Fizika Nebesnykh Tel*, **17**, 409
- Kiefer F., Lecavelier des Etangs A., Vidal-Madjar A., 2014a, in Ballet J., Martins F., Bournaud F., Monier R., Reylé C., eds, *SF2A-2014: Proceedings of the Annual meeting of the French Society of Astronomy and Astrophysics*. pp 39–43
- Kiefer F., Lecavelier des Etangs A., Boissier J., Vidal-Madjar A., Beust H., Lagrange A.-M., Hébrard G., Ferlet R., 2014b, *Nature*, **514**, 462
- Kiefer F., Lecavelier des Etangs A., Augereau J.-C., Vidal-Madjar A., Lagrange A.-M., Beust H., 2014c, *A&A*, **561**, L10
- Kóspál Á., Moór A., 2016, in Kastner J. H., Stelzer B., Metchev S. A., eds, *IAU Symposium Vol. 314, Young Stars & Planets Near the Sun*. pp 183–188 ([arXiv:1510.03618](https://arxiv.org/abs/1510.03618)), doi:10.1017/S1743921315006614
- Kóspál Á., et al., 2013, *ApJ*, **776**, 77
- Kral Q., Clarke C., Wyatt M., 2017a, preprint, ([arXiv:1703.08560](https://arxiv.org/abs/1703.08560))
- Kral Q., Matrá L., Wyatt M. C., Kennedy G. M., 2017b, *MNRAS*, **469**, 521
- Kuschnig R., Paunzen E., Weiss W. W., 1994, *Information Bulletin on Variable Stars*, **4070**
- Lyra W., Kuchner M., 2013, *Nature*, **499**, 184
- Marino S., et al., 2016, *MNRAS*, **460**, 2933
- Marino S., et al., 2017, *MNRAS*, **465**, 2595
- Mashonkina L. I., Shimanskiĭ V. V., Sakhbullin N. A., 2000, *Astronomy Reports*, **44**, 790
- Matthews B. C., Krivov A. V., Wyatt M. C., Bryden G., Eiroa C., 2014, *Protostars and Planets VI*, pp 521–544
- Mayor M., et al., 2003, *The Messenger*, **114**, 20
- Milli J., et al., 2017, *A&A*, **599**, A108
- Mittal T., Chen C. H., Jang-Condell H., Manoj P., Sargent B. A., Watson D. M., Lisse C. M., 2015, *ApJ*, **798**, 87
- Montgomery S. L., Welsh B. Y., 2012, *PASP*, **124**, 1042

- Montgomery S. L., Welsh B. Y., 2017, *MNRAS*, **468**, L55
- Moór A., et al., 2011, *ApJ*, **740**, L7
- Moór A., et al., 2015, *MNRAS*, **447**, 577
- Morales F. Y., Bryden G., Werner M. W., Stapelfeldt K. R., 2016, *ApJ*, **831**, 97
- Morton D. C., 1991, *ApJS*, **77**, 119
- Nesvorný D., Vokrouhlický D., Dones L., Levison H. F., Kaib N., Morbidelli A., 2017, *ApJ*, **845**, 27
- Olofsson J., Juhász A., Henning T., Mutschke H., Tamanai A., Moór A., Ábrahám P., 2012, *A&A*, **542**, A90
- Plez B., 2013, in Cambresy L., Martins F., Nuss E., Palacios A., eds, SF2A-2013: Proceedings of the Annual meeting of the French Society of Astronomy and Astrophysics. pp 141–146
- Pontoppidan K. M., Salyk C., Bergin E. A., Brittain S., Marty B., Mousis O., Öberg K. I., 2014, *Protostars and Planets VI*, pp 363–385
- Przybilla N., Nieva M.-F., Butler K., 2011, in *Journal of Physics Conference Series*. p. 012015 ([arXiv:1111.1445](https://arxiv.org/abs/1111.1445)), doi:10.1088/1742-6596/328/1/012015
- Rebollido I., et al., 2018, preprint, ([arXiv:1801.07951](https://arxiv.org/abs/1801.07951))
- Redfield S., 2007, *ApJ*, **656**, L97
- Redfield S., Linsky J. L., 2008, *ApJ*, **673**, 283
- Rhee J. H., Song I., Zuckerman B., McElwain M., 2007, *ApJ*, **660**, 1556
- Riviere-Marichalar P., et al., 2012, *A&A*, **546**, L8
- Roberge A., Feldman P. D., Weinberger A. J., Deleuil M., Bouret J.-C., 2006, *Nature*, **441**, 724
- Roberge A., Welsh B. Y., Kamp I., Weinberger A. J., Grady C. A., 2014, *ApJ*, **796**, L11
- Savage B. D., Sembach K. R., 1991, *ApJ*, **379**, 245
- Sbordone L., Bonifacio P., Castelli F., Kurucz R. L., 2004, *Memorie della Societa Astronomica Italiana Supplementi*, **5**, 93
- Siess L., Dufour E., Forestini M., 2000, *A&A*, **358**, 593
- Sitnova T., Ryabchikova T., Alexeeva S., Mashonkina L., 2017, preprint, ([arXiv:1710.06726](https://arxiv.org/abs/1710.06726))
- Smette A., et al., 2015, *A&A*, **576**, A77
- Thébaud P., 2009, *A&A*, **505**, 1269
- Thébaud P., Beust H., 2001, *A&A*, **376**, 621
- Thi W. F., et al., 2013, *A&A*, **557**, A111
- Welsh B. Y., Montgomery S., 2013, *PASP*, **125**, 759
- Welsh B. Y., Montgomery S. L., 2015, *Advances in Astronomy*, **2015**, 980323
- Welsh B. Y., Montgomery S. L., 2018, *MNRAS*, **474**, 1515
- Wenger M., et al., 2000, *A&AS*, **143**, 9
- Werner M. W., et al., 2004, *ApJS*, **154**, 1
- Williams J. P., Best W. M. J., 2014, *ApJ*, **788**, 59
- Williams J. P., Cieza L. A., 2011, *ARA&A*, **49**, 67
- Wilson R. E., 1953, *Carnegie Institute Washington D.C. Publication*,
- Wyatt M. C., 2008, *ARA&A*, **46**, 339
- Wyatt M. C., Panić O., Kennedy G. M., Matrà L., 2015, *Ap&SS*, **357**, 103
- Zorec J., Royer F., 2012, *A&A*, **537**, A120
- van Leeuwen F., 2007, *A&A*, **474**, 653

APPENDIX A: PHOTOSPHERIC LINE FITS

In this appendix we provide the Figures illustrating the Kurucz models that best reproduce each one of the lines of the reference spectrum for each star in the sample. In all cases the reference spectrum is displayed in black and the best fitting model in red. Please note that the parameters are allowed to vary between different lines for the same object (as these models do not include non-LTE effects).

APPENDIX B: RESIDUAL COMPONENTS

In this appendix we provide the Figures showing every isolated component and the multi-gaussian fit obtained to reproduce and characterize those features.

APPENDIX C: NEIGHBOURING STARS

In this appendix we show the analysis performed with neighbouring stars looking for features of similar characteristics to those detected in each “science” target (paying particular attention to the velocity). The detection of the same feature in several stars does automatically support an ISM origin of the feature.

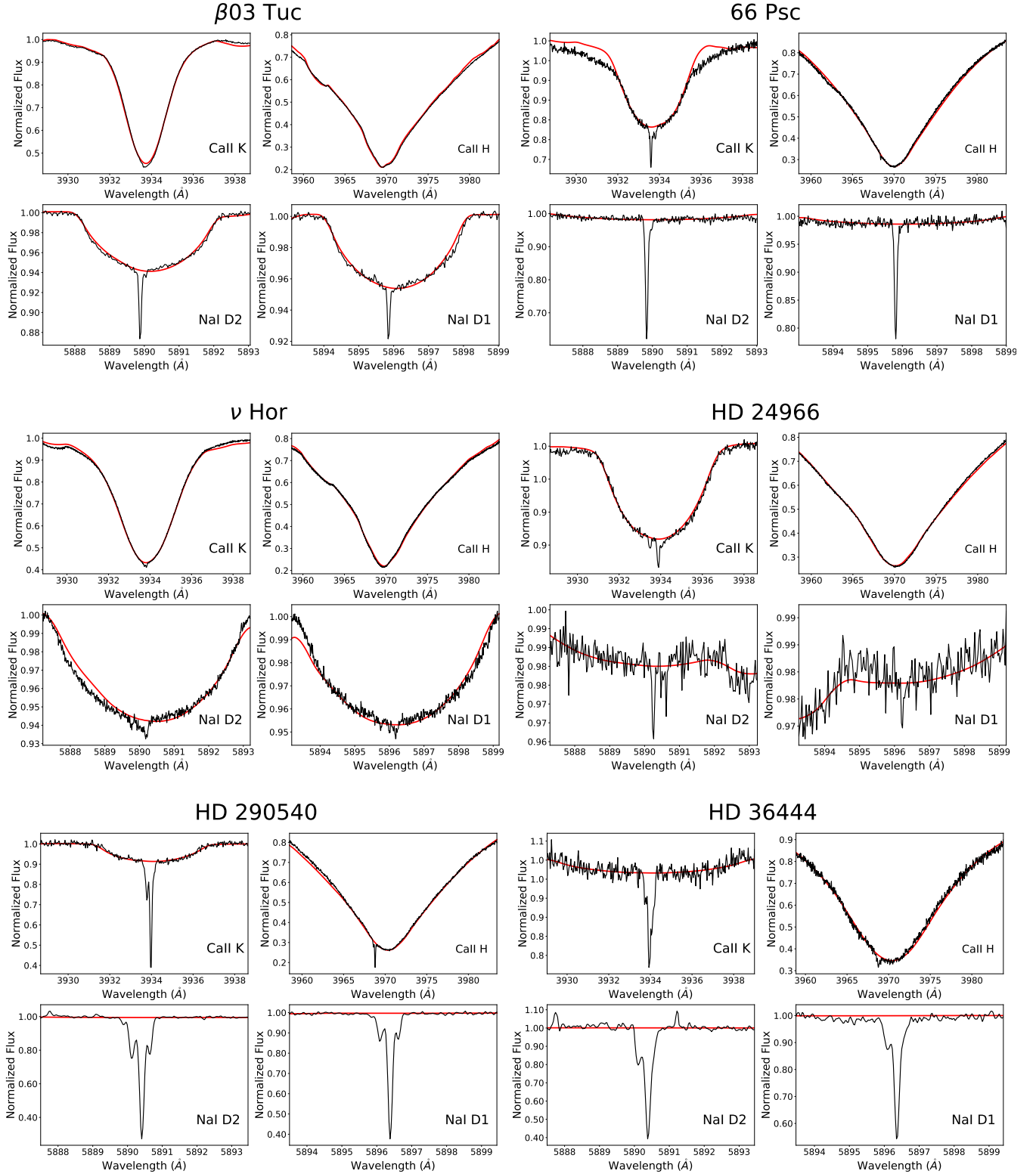


Figure A1. Best-fit models for $\beta 03$ Tuc's, 66 Psc's, ν Hor's, HD 24966's, HD 290540's and HD 36444's Ca II H&K and Na I D1&D2 lines. Median from the real spectra in black, synthetic spectrum in red.

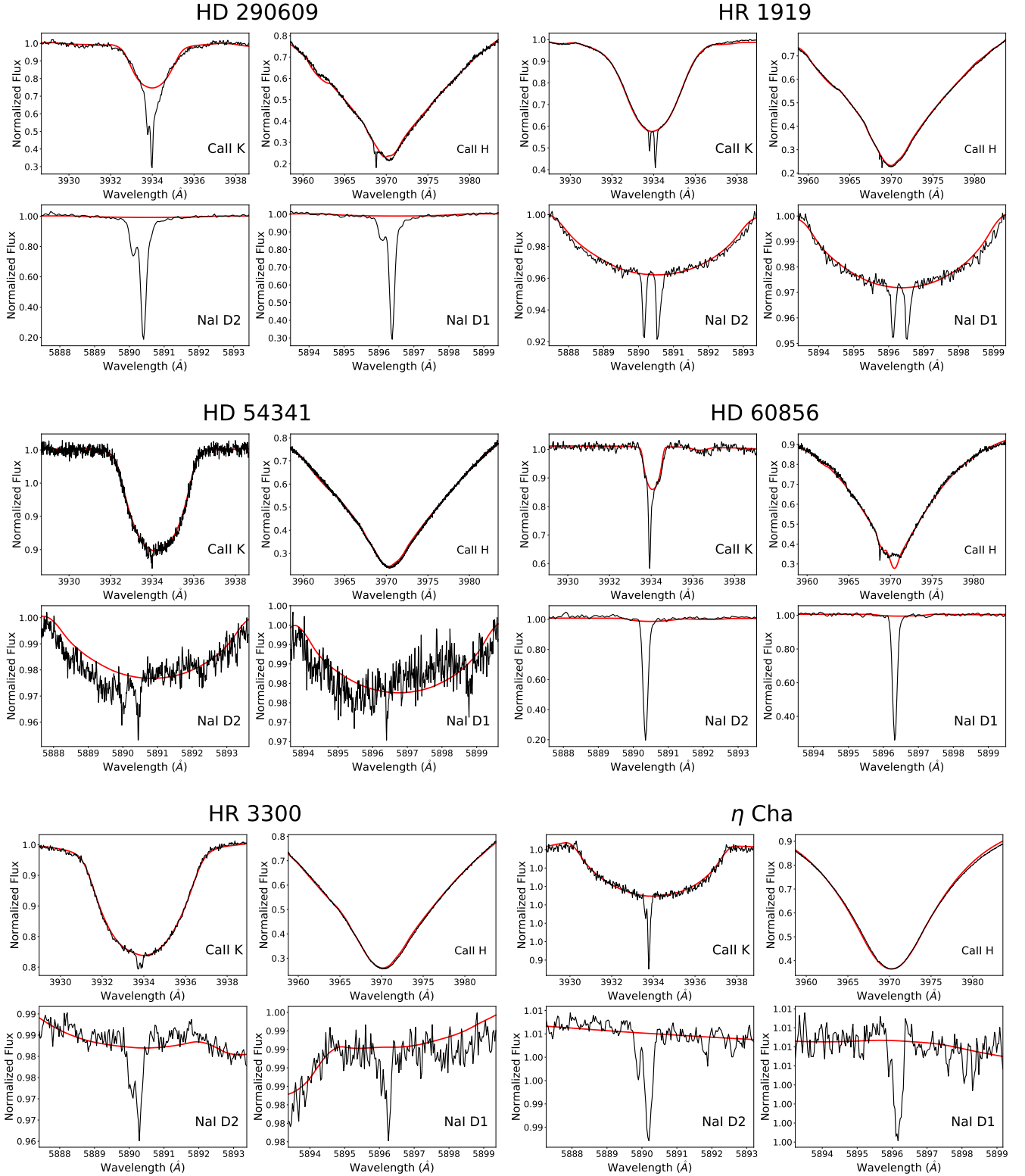


Figure A2. Best-fit models for HD 290609's, HR 1919's, HD 54341's, HD 60856's, HR 3300's and η Cha's Ca II H&K and Na I D1&D2 lines. Median from the real spectra in black, synthetic spectrum in red.

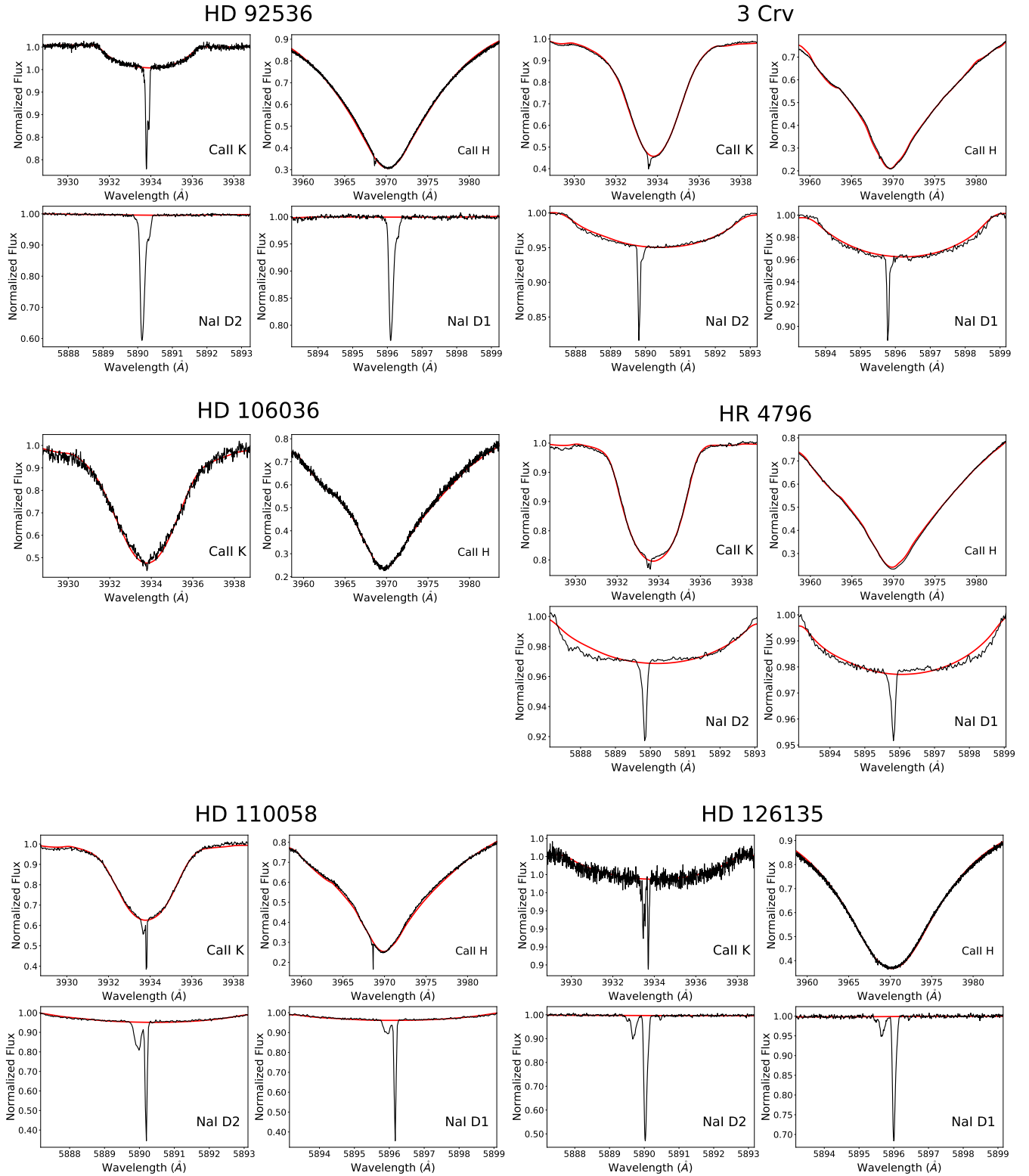


Figure A3. Best-fit models for HD 92536's, 3 Crv's, HD 106036's, HR 4796's, HD 110058's and HD 126235's Ca II H&K and Na I D1&D2 lines. Median from the real spectra in black, synthetic spectrum in red.

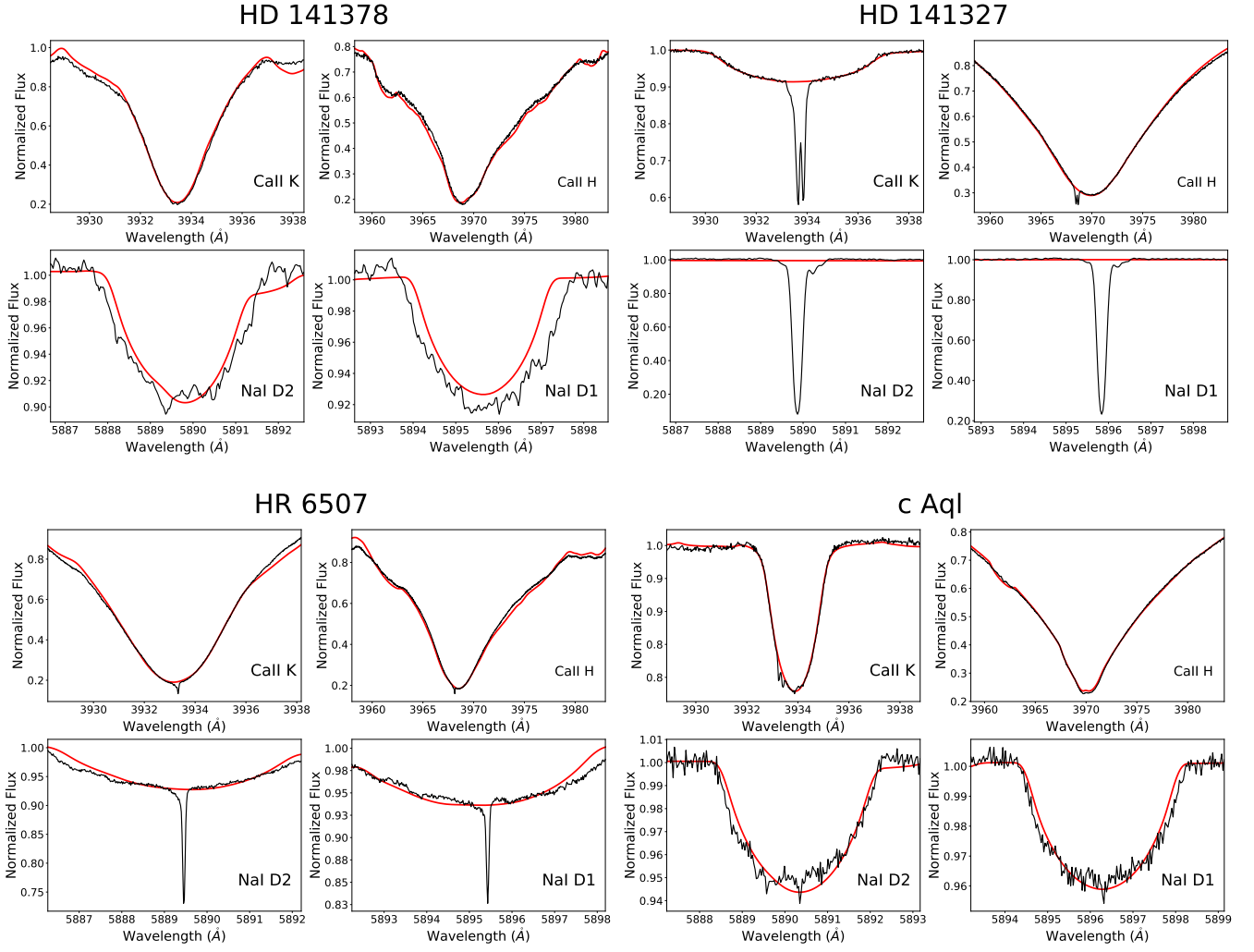


Figure A4. Best-fit models for HD 141378's, HD 141327's, HR 6507 and c Aql's Ca II H&K and Na I D1&D2 lines. Median from the real spectra in black, synthetic spectrum in red.

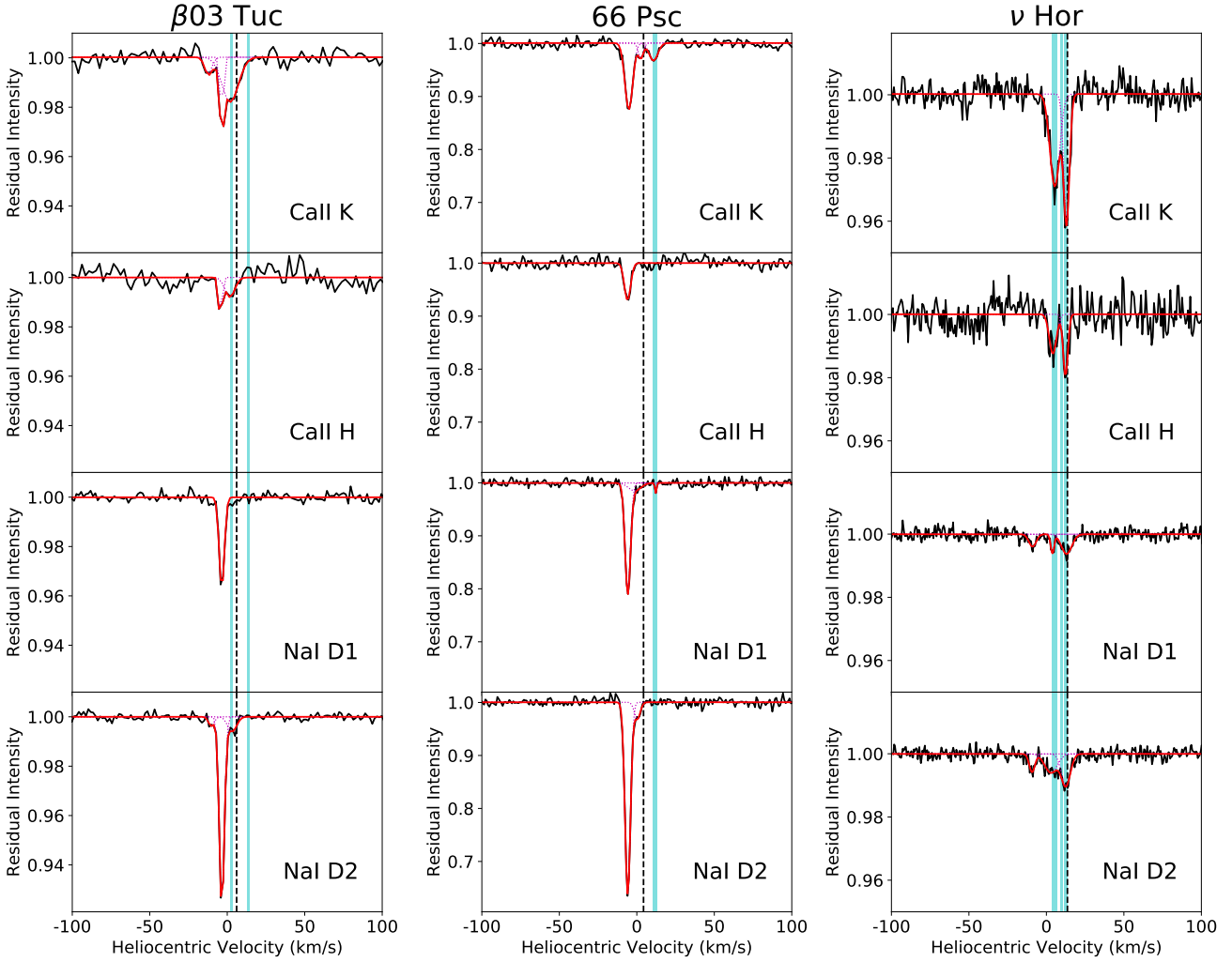


Figure B1. Absorption profiles of the Ca II H & K and Na I D1 & D2 lines for $\beta 03$ Tuc, 66 Psc and ν Hor. Photospheric absorptions has been subtracted and the remaining extra components have been modelled by gaussian profiles. Individual gaussian fits are shown in dotted magenta lines and the combined profile is shown in red. Dashed black line marks the estimated radial velocity of the star and cyan lines mark the velocity of the traversing clouds in the line of sight with their respective errors as their line widths.

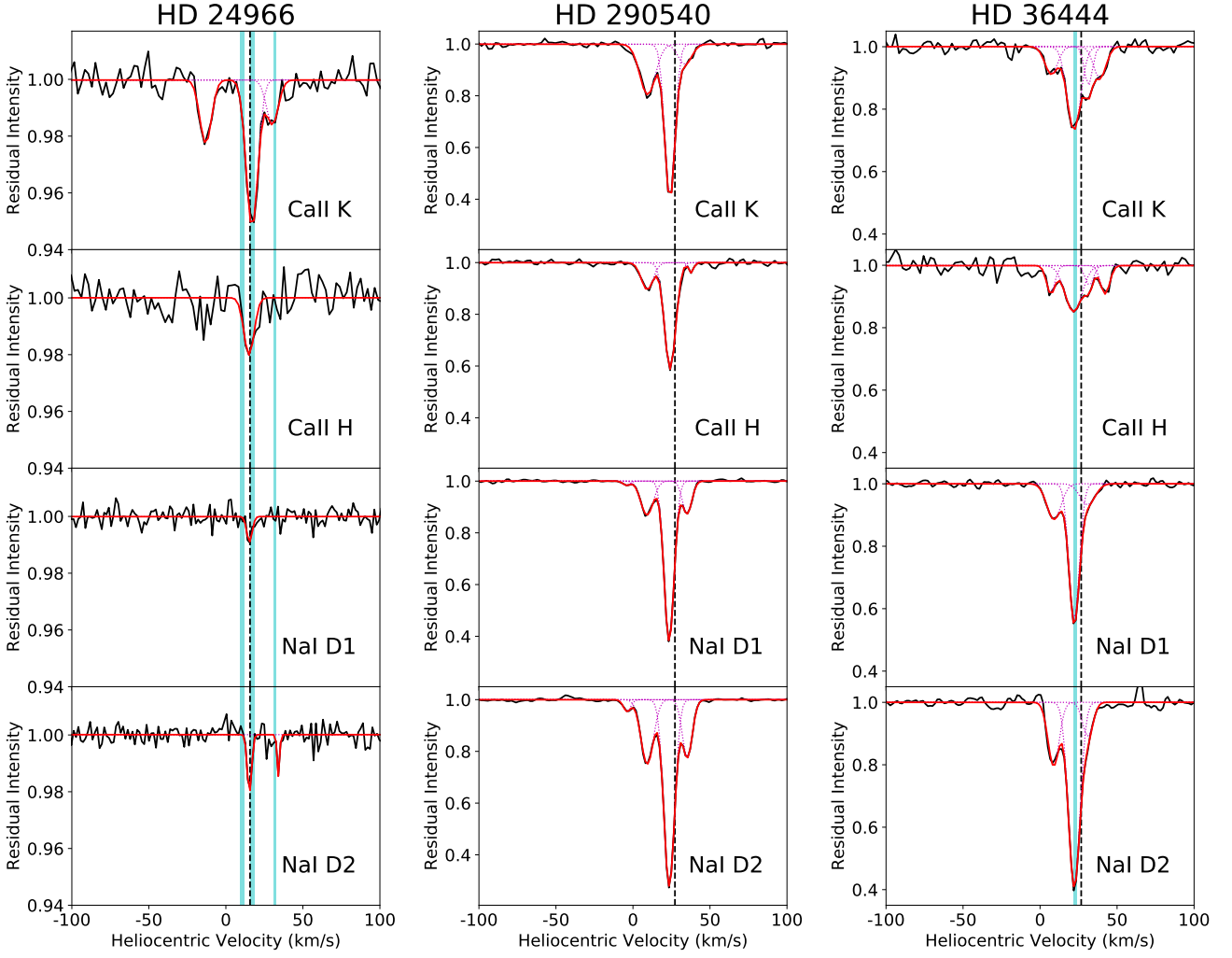


Figure B2. Absorption profiles of the Ca II H & K and Na I D1 & D2 lines for HD 24966, HD 290540 and HD 36444. Photospheric absorptions has been subtracted and the remaining extra components have been modelled by gaussian profiles. Individual gaussian fits are shown in dotted magenta lines and the combined profile is shown in red. Dashed black line marks the estimated radial velocity of the star and cyan lines mark the velocity of the traversing clouds in the line of sight with their respective errors as their line widths.

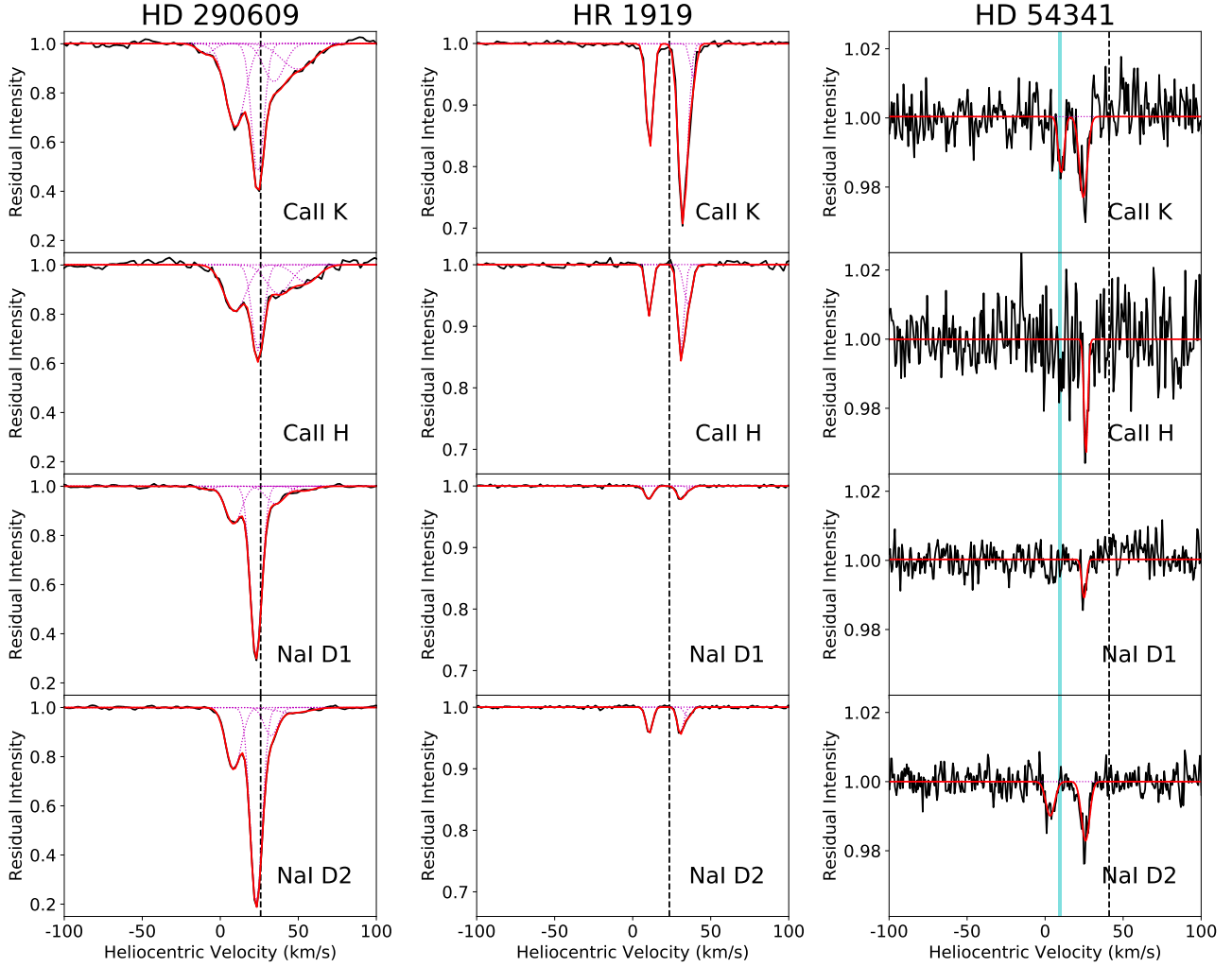


Figure B3. Absorption profiles of the Ca II H & K and Na I D1 & D2 lines for HD 290609, HR 1919 and HD 54341. Photospheric absorptions has been subtracted and the remaining extra components have been modelled by gaussian profiles. Individual gaussian fits are shown in dotted magenta lines and the combined profile is shown in red. Dashed black line marks the estimated radial velocity of the star and cyan lines mark the velocity of the traversing clouds in the line of sight with their respective errors as their line widths.

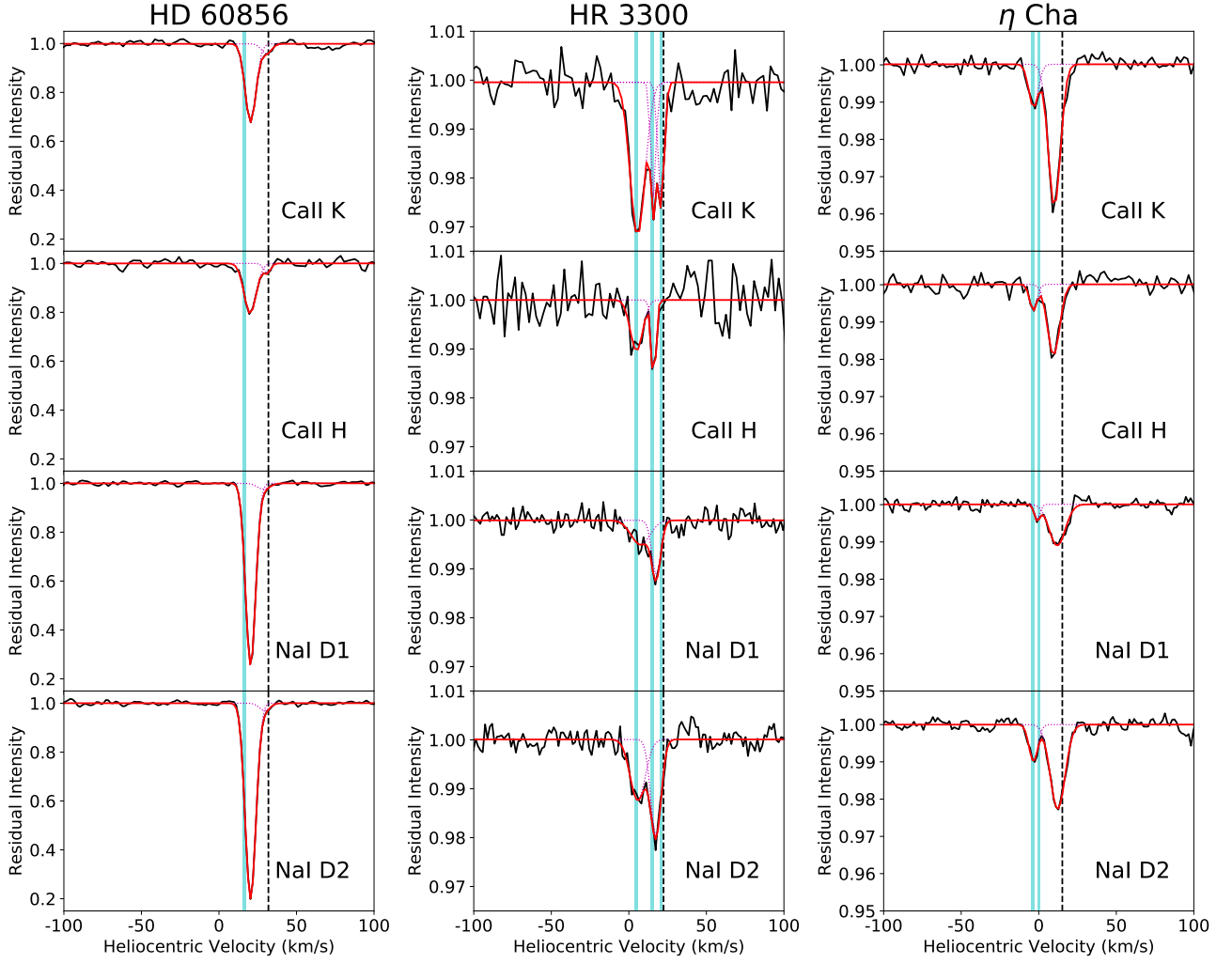


Figure B4. Absorption profiles of the Ca II H & K and Na I D1 & D2 lines for HD 60856, HR 3300 and η Cha. Photospheric absorptions has been subtracted and the remaining extra components have been modelled by gaussian profiles. Individual gaussian fits are shown in dotted magenta lines and the combined profile is shown in red. Dashed black line marks the estimated radial velocity of the star and cyan lines mark the velocity of the traversing clouds in the line of sight with their respective errors as their line widths.

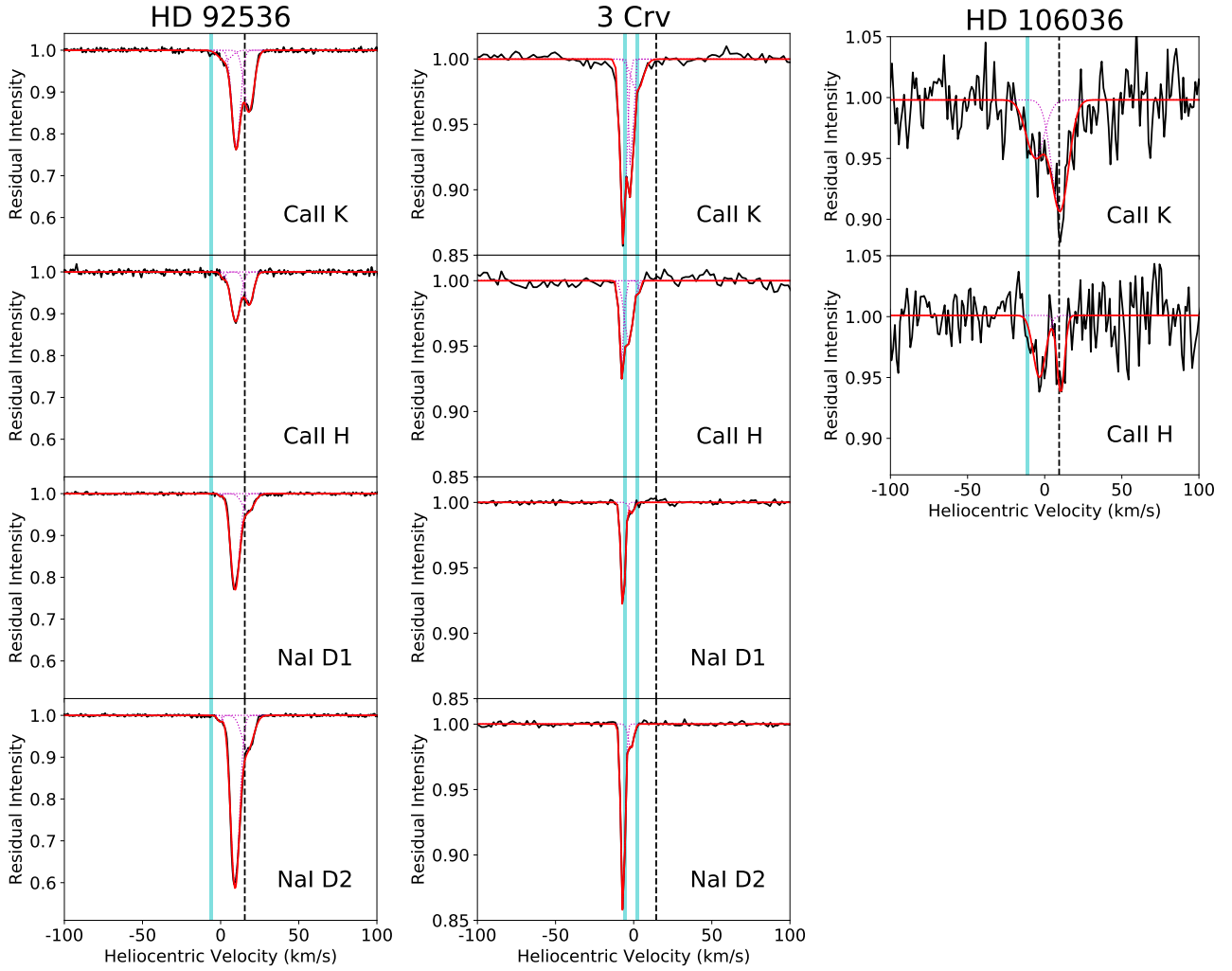


Figure B5. Absorption profiles of the Ca II H & K and Na I D1 & D2 lines for HD 92536, 3 Crv and HD 106036. Photospheric absorptions has been subtracted and the remaining extra components have been modelled by gaussian profiles. Individual gaussian fits are shown in dotted magenta lines and the combined profile is shown in red. Dashed black line marks the estimated radial velocity of the star and cyan lines mark the velocity of the traversing clouds in the line of sight with their respective errors as their line widths.

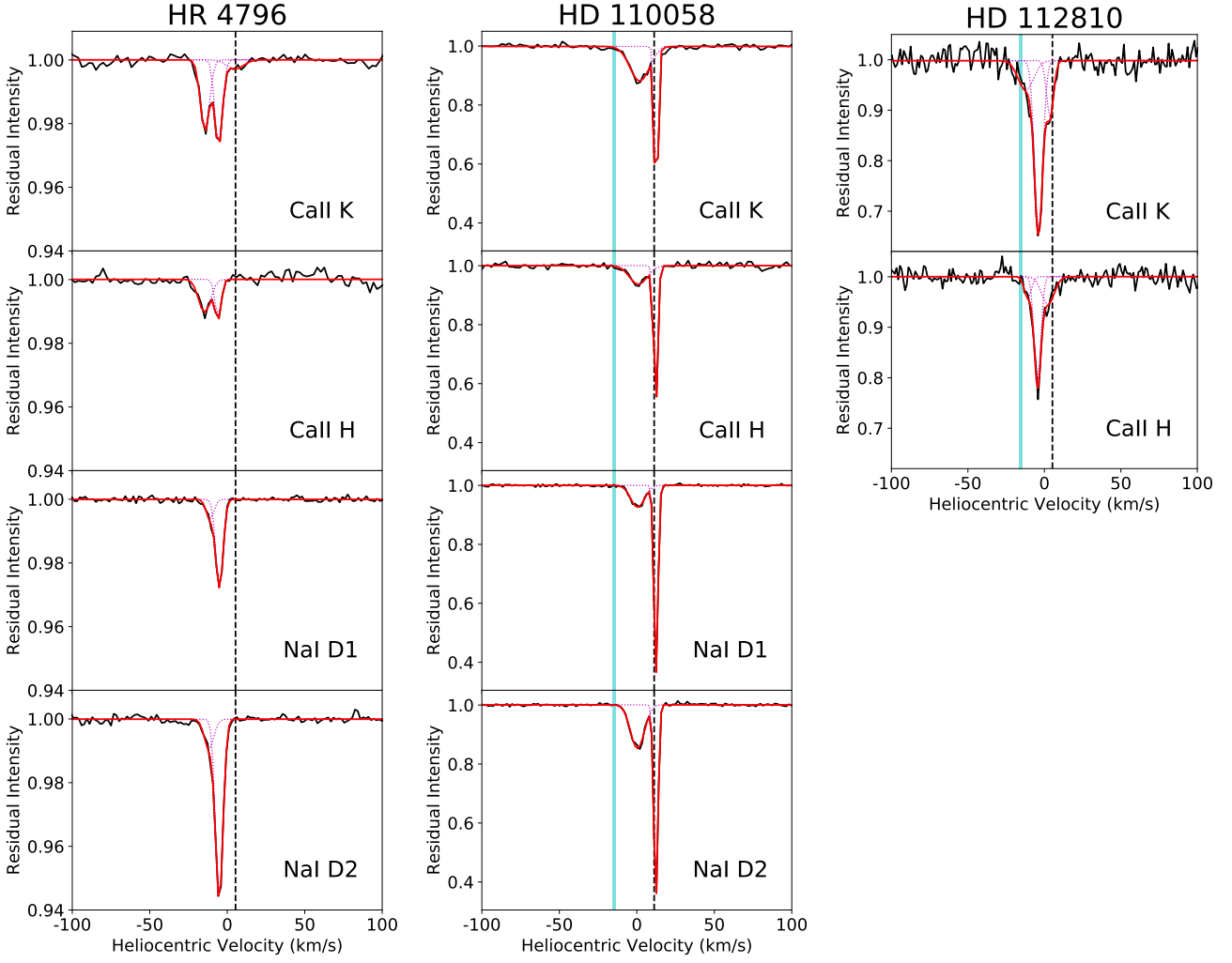


Figure B6. Absorption profiles of the Ca II H & K and Na I D1 & D2 lines for HR 4796, HD 110058 and HD 112810. Photospheric absorptions has been subtracted and the remaining extra components have been modelled by gaussian profiles. Individual gaussian fits are shown in dotted magenta lines and the combined profile is shown in red. Dashed black line marks the estimated radial velocity of the star and cyan lines mark the velocity of the traversing clouds in the line of sight with their respective errors as their line widths.

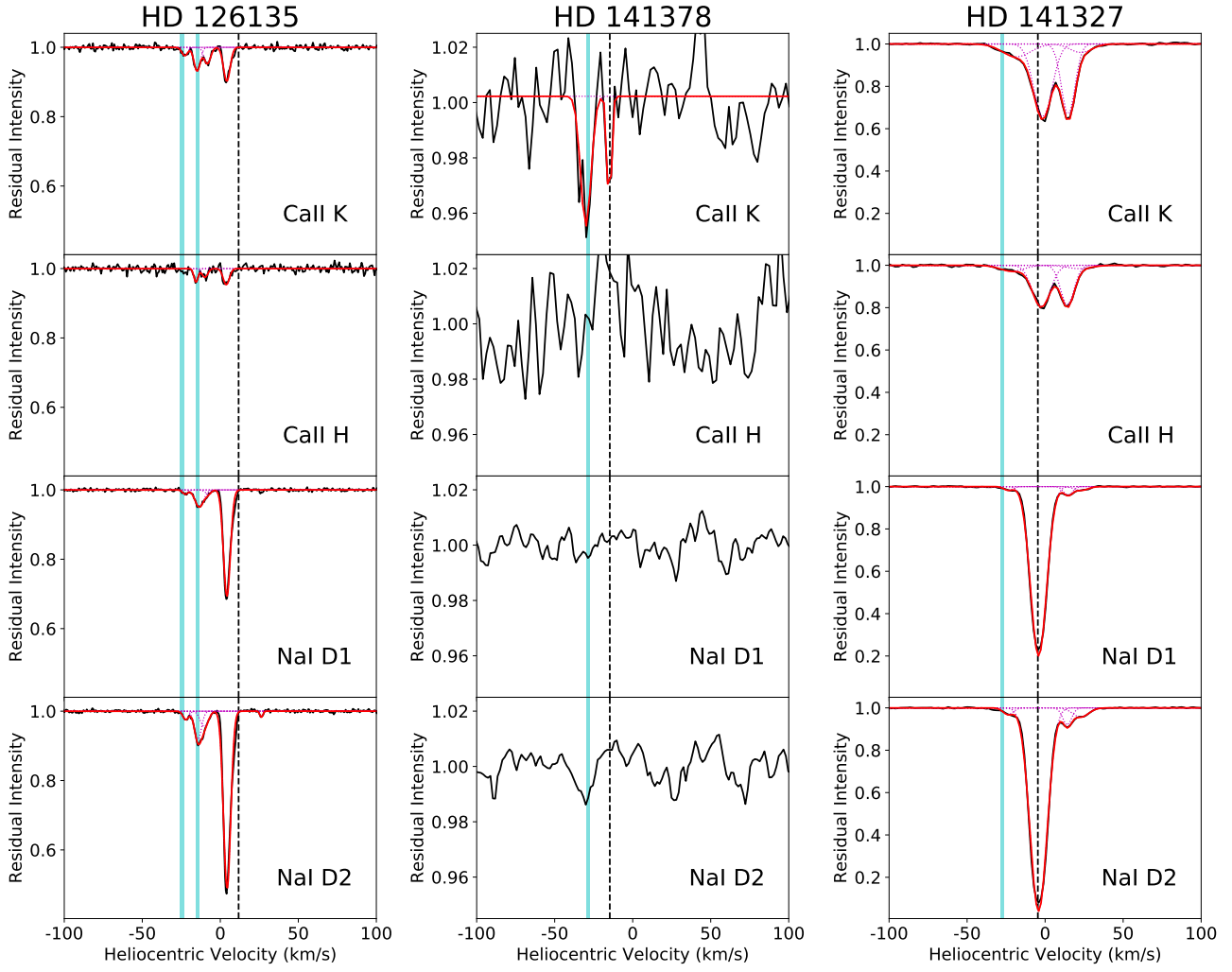


Figure B7. Absorption profiles of the Ca II H & K and Na I D1 & D2 lines for HD 126135, HD 141378 and HD 141327. Photospheric absorptions has been subtracted and the remaining extra components have been modelled by gaussian profiles. Individual gaussian fits are shown in dotted magenta lines and the combined profile is shown in red. Dashed black line marks the estimated radial velocity of the star and cyan lines mark the velocity of the traversing clouds in the line of sight with their respective errors as their line widths.

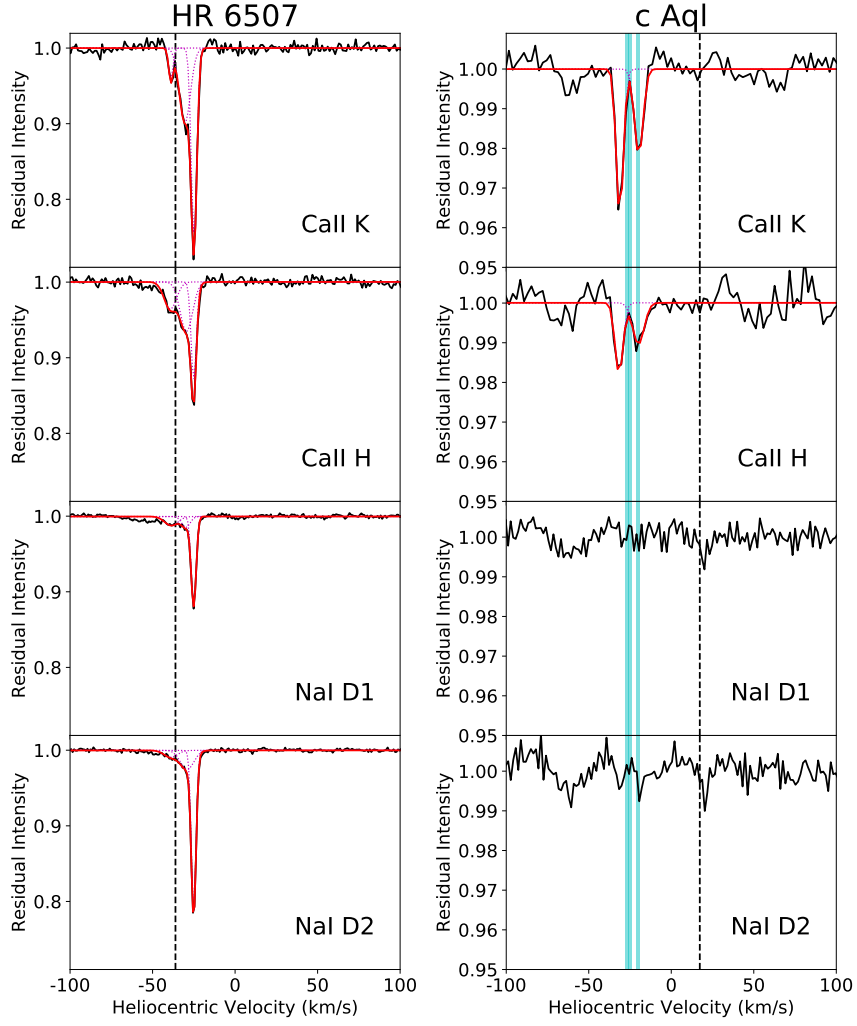


Figure B8. Absorption profiles of the Ca II H & K and Na I D1 & D2 lines for HR 6507 and c Aql. Photospheric absorptions has been subtracted and the remaining extra components have been modelled by gaussian profiles. Individual gaussian fits are shown in dotted magenta lines and the combined profile is shown in red. Dashed black line marks the estimated radial velocity of the star and cyan lines mark the velocity of the traversing clouds in the line of sight with their respective errors as their line widths.

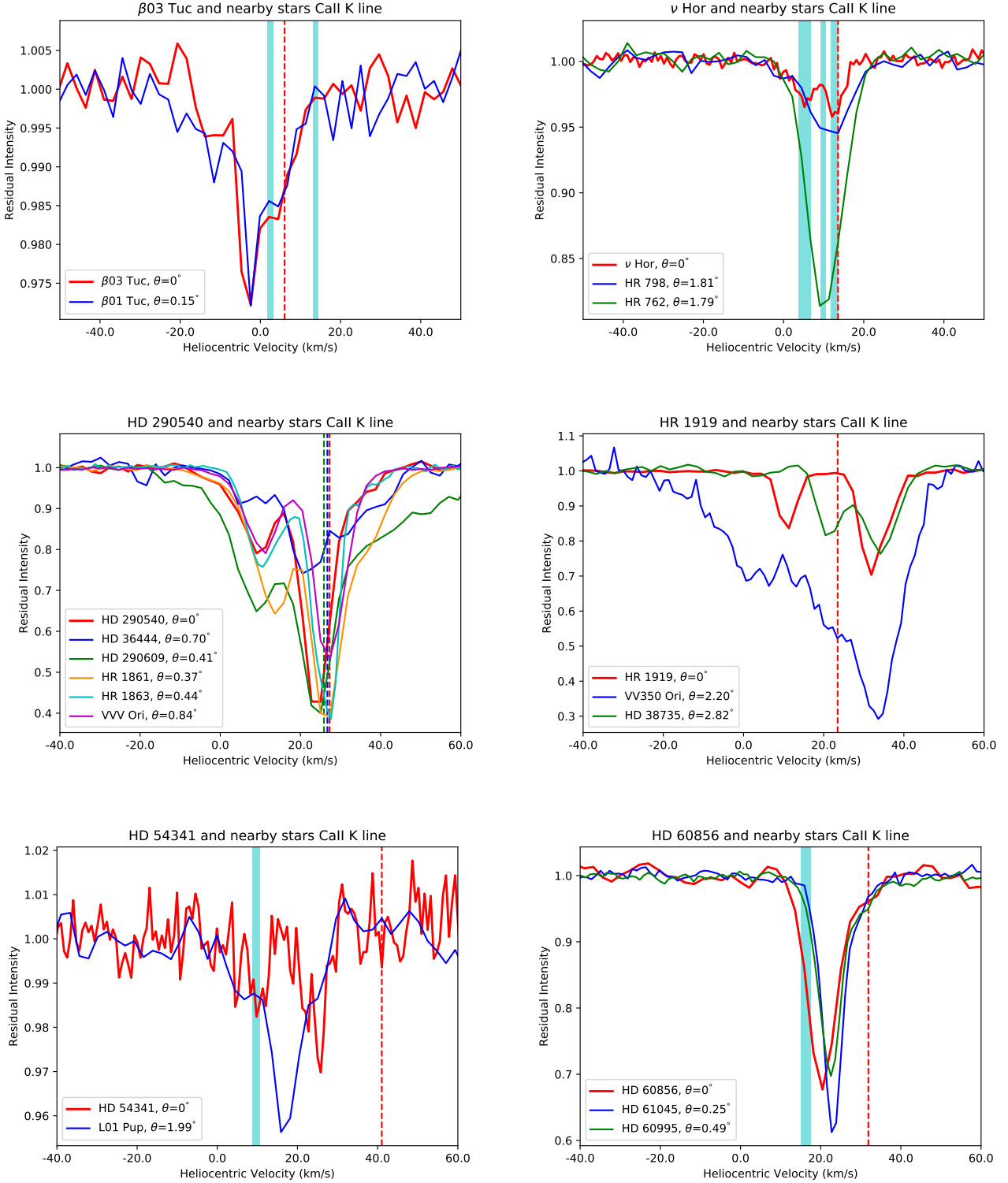


Figure C1. Nearby stars around $\beta 03$ Tuc, ν Hor, HD 290540 (along with HD 36444 and HD 290609), HR1919, HD 54341 and HD 60856. Dashed line marks the estimated radial velocity of the star and cyan lines mark the velocity of the traversing clouds in the line of sight with their respective errors as their line widths.

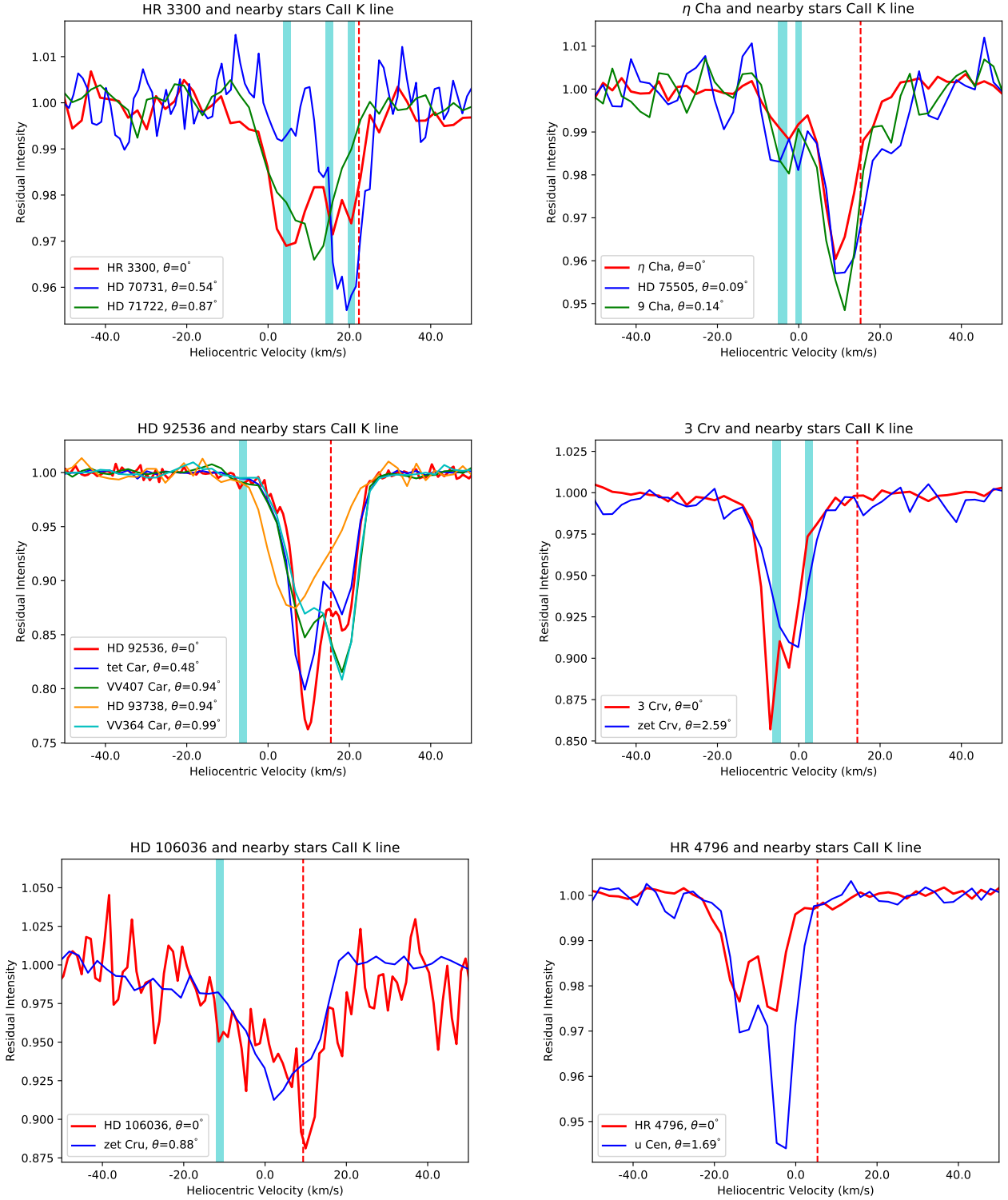


Figure C2. Nearby stars around HR 3300, η Cha, HD 92536, 3 Crv, HD 106036 and HR 4796. Dashed line marks the estimated radial velocity of the star and cyan lines mark the velocity of the traversing clouds in the line of sight with their respective errors as their line widths.

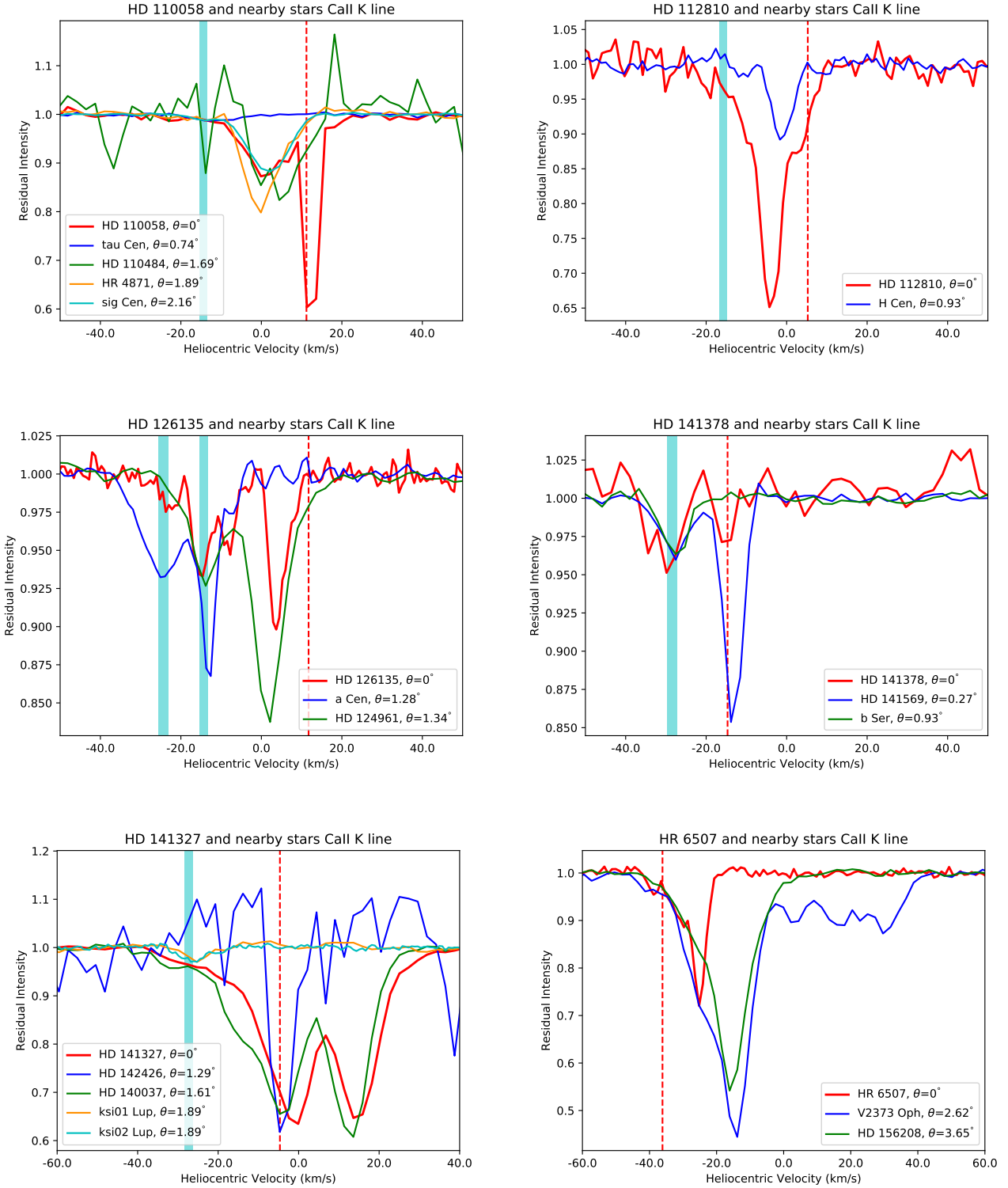


Figure C3. Nearby stars around HD 110058, HD 112810, HD 126135, HD 141378, HD 141327 and HR 6507. Dashed line marks the estimated radial velocity of the star and cyan lines mark the velocity of the traversing clouds in the line of sight with their respective errors as their line widths.

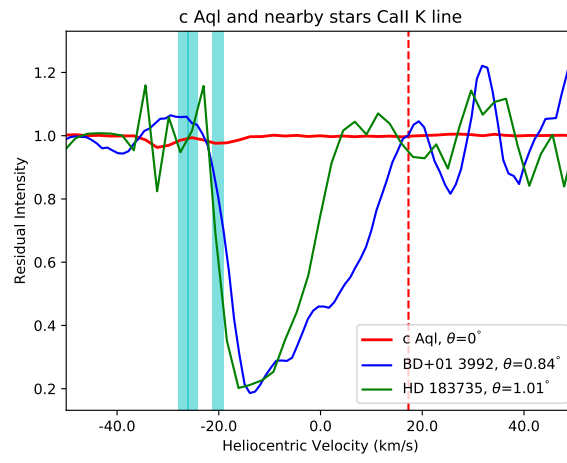


Figure C4. Nearby stars around c Aql. Dashed line marks the estimated radial velocity of the star and cyan lines mark the velocity of the traversing clouds in the line of sight with their respective errors as their line widths.

Table C1: All nearby stars used in the analysis per each object of science, their number of spectra, instrument and ESO program ID. Note that HD 290540, HD 36444 and HD 290609 are each other's nearby stars and in addition have three other common nearby stars.

Object	Nearby star	Number of Spectra	Instrument	Program ID
β 03 Tuc	β 01 Tuc	6	HARPS	073.C-0733(E)
		2	HARPS	075.C-0689(A)
		2	HARPS	077.C-0295(A)
		2	HARPS	077.C-0295(B)
		3	FEROS	094.A-9012(A)
ν Hor	HR 798	1	FEROS	179.C-0197(B)
	HR 762	4	FEROS	088.C-0498(A)
HD 290540, HD 36444 and HD 290609	HR 1861	1	FEROS	074.B-0455(A)
	HR 1863	12	UVES	266.D-5655(A)
	VVV Ori	98	UVES	194.C-0833(C)
		6	FEROS	096.A-9030(A)
		2	FEROS	096.A-9024(A)
HR 1919	VV350 Ori	2	UVES	082.C-0831(A)
	HD 38735	79	FEROS	084.C-1008(A)
		24	FEROS	084.A-9004(B)

Continued on next page

Table C1 – continued from previous page

Object	Nearby star	Number of Spectra	Instrument	Program ID
		4	FEROS	091.D-0414(B)
HD 54341	L01 Pup	1	FEROS	088.A-9003(A)
HD 60856	HD 61045	8	UVES	072.D-0410(A)
	HD 60995	6	UVES	098.C-0463(A)
HR 3300	HD 70731	7	UVES	093.D-0852(A)
	HD 71722	5	HARPS	094.C-0946(A)
		12	FEROS	094.A-9012(A)
η Cha	HD 75505	7	FEROS	084.A-9003(A)
		1	FEROS	086.A-9006(A)
	9 Cha	310	FEROS	078.D-0549(A)
		3	FEROS	084.A-9003(A)
HD 92536	tet Car	1	FEROS	073.D-0291(A)
		1	FEROS	074.D-0300(A)
		15	UVES	076.C-0503(A)
		80	UVES	077.C-0547(A)
		1	FEROS	078.D-0080(A)
		125	UVES	194.C-0833(A)
	VV407 Car	9	FEROS	086.D-0449(A)
	HD 93738	2	FEROS	096.A-9018(A)
	VV364 Car	6	FEROS	086.D-0449(A)
3 Crv	zet Crv	1	FEROS	179.C-0197(D)
HD 106036	zet Cru	1	FEROS	090.D-0358(A)
HR 4796	u Cen	30	FEROS	60.A-9700(A)
		121	HARPS	60.A-9036(A)
		120	HARPS	60.A-9700(G)
HD 110058	tau Cen	8	HARPS	076.C-0279(A)
		4	HARPS	076.C-0279(C)
		1	FEROS	078.D-0080(A)
		20	UVES	087.D-0010(A)
	HD 110484	3	FEROS	083.C-0139(A)
	HR 4871	1	FEROS	078.D-0080(A)
		1	FEROS	087.C-0227(C)
		13	HARPS	088.C-0353(A)
		13	HARPS	089.C-0006(A)
	sig Cen	1	FEROS	082.B-0484(A)
		40	FEROS	084.B-0029(A)
HD 112810	H Cen	10	UVES	266.D-5655(A)
		2	HARPS	185.D-0056(A)
		1	HARPS	185.D-0056(C)
HD 126135	a Cen	14	UVES	266.D-5655(A)
		64	UVES	073.D-0504(A)
		3	HARPS	075.C-0234(A)
		3	HARPS	079.C-0170(A)
		18	UVES	081.C-0475(A)
		4	UVES	097.D-0035(A)
	HD 124961	2	FEROS	072.D-0021(A)
		2	FEROS	073.D-0049(A)
		2	FEROS	082.D-0061(A)
HD 141378	HD 141569	1	UVES	075.C-0637(A)
		109	UVES	079.C-0789(A)
		1	FEROS	083.A-9003(A)
		7	FEROS	085.A-9027(B)
	b Ser	10	UVES	076.B-0055(A)
		8	HARPS	077.C-0295(A)
		2	HARPS	077.C-0295(C)
		2	FEROS	083.A-9014(A)
		2	FEROS	083.A-9011(B)
		1	FEROS	083.A-9014(B)
		3	FEROS	084.A-9011(B)

Continued on next page

Table C1 – continued from previous page

Object	Nearby star	Number of Spectra	Instrument	Program ID	
HD 141327	HD 142426	3	FEROS	085.A-9027(G)	
		6	FEROS	089.D-0097(B)	
		2	FEROS	090.D-0061(B)	
	HD 140037	2	FEROS	091.D-0145(A)	
		1	FEROS	179.C-0197(C)	
	ksi01 Lup	1	FEROS	091.C-0713(A)	
		11	FEROS	075.D-0342(A)	
		6	HARPS	075.C-0689(A)	
		2	HARPS	075.C-0689(B)	
		2	HARPS	077.C-0295(D)	
		ksi02 Lup	2	HARPS	075.C-0689(B)
			2	HARPS	077.C-0295(D)
		2	HARPS	077.C-0295(C)	
	12	HARPS	184.C-0815(F)		
HR 6051	HD 146029	1	FEROS	179.C-0197(A)	
	HD 144822	1	FEROS	077.C-0138(A)	
HR 6507	V2373 Oph	9	FEROS	091.D-0122(A)	
	HD 156208	8	FEROS	081.D-2002(A)	
c Aql	BD+01 3992	10	UVES	293.D-5036(A)	
	HD 183735	1	FEROS	083.D-0034(A)	

This paper has been typeset from a $\text{\TeX}/\text{\LaTeX}$ file prepared by the author.